Mineralium Deposita (2019) 54:347–368
https://doi.org/10.1007/s00126-018-0811-7

ARTICLE

The shear zone-related gold mineralization at the Turmalina deposit, Quadrilátero Ferrífero, Brazil: structural evolution and the two stages of mineralization

Wendell Fabricio-Silva[1,2] · Carlos Alberto Rosière[1] · Bernhard Bühn[2]

Received: 24 August 2016 / Accepted: 30 April 2018 / Published online: 16 May 2018

Abstract

Turmalina is an important orogenic gold deposit located in the NW region of the Quadrilátero Ferrífero. The deposit is hosted in an Archean greenstone belt composed of ortho-amphibolites and pelites with interleaved tuffs metamorphosed under amphibolite facies conditions and intruded by a granite stock. The orebodies are controlled by WNW-ESE-trending shear zones, associated with hydrothermal alteration. Three deformation events are recognized in the Turmalina gold deposit: D_1 and D_2 are the result of a progressive Archean deformation under ductile conditions between 2749 ± 7 and 2664 ± 35 Ma; D_3 is characterized by a transpressional event under ductile-brittle conditions with the age still unclear. The three generations of garnet observed show that Grt_1 blastesis is pre- to syn-D_1 and Grt_2 growth during the late to post-deformation stages of the D_2 event. The initial temperature (Grt_1 core) is around 548–600 °C, whereas during late D_2, the temperatures reached 633 °C (metamorphic peak–Grt_2 rim), likely as a result of granite intrusion. The Grt_3 resulted from re-equilibration under retrograde conditions. Two gold-bearing sulfide stages were identified: pyrrhotite-arsenopyrite ± löllingite ± chalcopyrite ± gold stage I precipitated below a metamorphic peak temperature of 598 ± 19 °C associated with S_1 foliation (D_1), and pyrrhotite-pyrite-arsenopyrite ± chalcopyrite ± gold stage II is located commonly along V_3 quartz-carbonate veinlets with a temperature range between 442 ± 9 and 510 ± 30 °C. We suggest that the granite intrusion imposed an additional thermal effect that promoted further dehydration of country rocks. The Au derived mainly from a metamorphic fluid source but potentially mixed with magmatic fluids from the granite.

Keywords Archean greenstone belt · Quadrilátero Ferrífero · Turmalina deposit · Gold · Structural evolution · Sulfur isotopes

Introduction

The Turmalina orogenic gold deposit is hosted in an Archean greenstone belt in the NW area of the Quadrilátero Ferrífero (translated as "Iron Quadrangle"), Minas Gerais, Brazil (Fig. 1a). The Quadrilátero Ferrífero (QF) is an important Brazilian mining district located in the southern São Francisco Craton (Almeida 1977; Inda et al. 1984) and contains one of the largest Fe and Au metallogenic provinces in the world (Thorman et al. 2001). In the Turmalina region, the geological units are correlated and were subject to a comparable tectonic evolution, with the Rio das Velhas greenstone belt. Frizzo et al. (1991) and Soares et al. (2017) renamed the volcano-sedimentary sequences in the NW of the QF into the Pitangui greenstone belt. Currently, this region is the target for gold mineralization associated with the tectonic lineaments Pitangui and Penha-Onça (Fig. 1).

In the QF greenstone belts, gold orebodies are structurally controlled and associated with hydrothermal alteration along regional-scale shear zones (Baltazar and Zucchetti 2007). The gold mineralization is epigenetic, mostly related to quartz-carbonate veins, and is associated with sulfide enrichment in the wall rocks (Lobato et al. 2001). Although the main host units in these greenstone belts are banded iron formations

Editorial handling: S. Hagemann

Electronic supplementary material The online version of this article (https://doi.org/10.1007/s00126-018-0811-7) contains supplementary material, which is available to authorized users.

✉ Wendell Fabricio-Silva
wendellfabricio@gmail.com

[1] Universidade Federal de Minas Gerais, Belo Horizonte, Minas Gerais 31270-901, Brazil

[2] Universidade de Brasília, Brasília, Distrito Federal 70910-900, Brazil

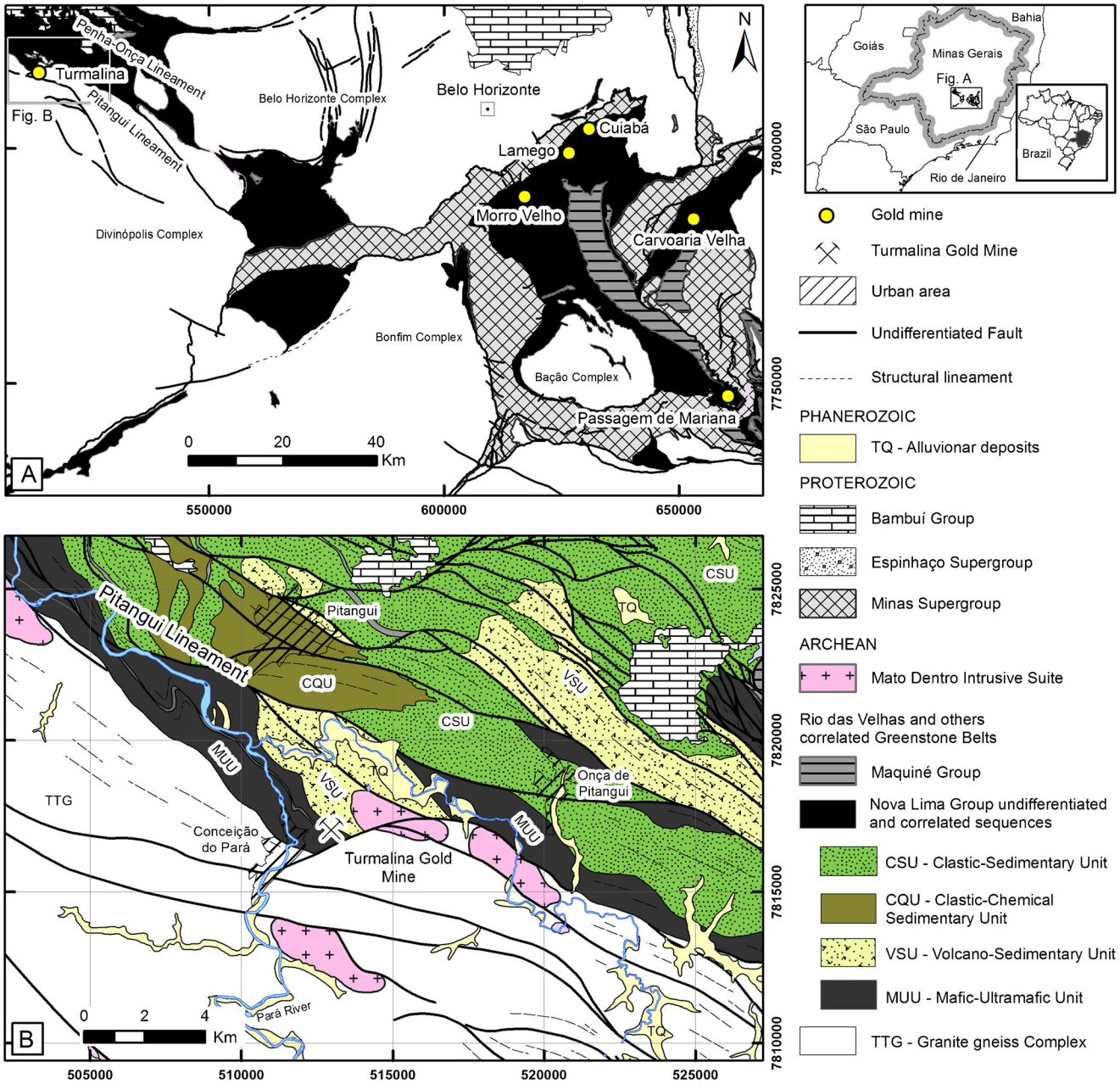

Fig. 1 **a** Schematic geological map of the Quadrilátero Ferrífero (Minas Gerais, Brazil) showing the Rio das Velhas and other correlated greenstone belts, as well as some of the major gold mines. Compiled and adapted after Dorr (1969) and Renger et al. (1994). **b** Map of the Pitangui geological region (modified and adapted after Romano 2006)

(BIFs) (Vial et al. 2007a), gold in the Turmalina deposit is hosted in meta-mafic/ultramafic and volcano-clastic rocks.

The deposit comprises two shear zone-controlled orebodies (A and B) (Fig. 2). They are approximately parallel to each other, WNW-ESE striking and dipping ca. 60° to the NE. Orebody A is about 250 m long, with an average thickness of 6 m and an average gold grade of 5 g/t. Orebody B is about 300 m long and has an average thickness of 3 m with a gold content of about 4 g/t. The Turmalina Mining Corporation, which belongs to Jaguar Mining, Inc., is currently the holder of four gold exploration areas in the Pitangui lineament. In 2016, the total measured and indicated gold resources in the Turmalina Project were 540,000 oz with a grade of 4.93 g/t Au (Jaguar Mining 2017).

The processes of hydrothermal alteration, mineralization, and metamorphism in Turmalina were first studied by Frizzo et al. (1991) and Oliveira (2012). Later, Velasquez David (2011) and Tassinari et al. (2015) presented geochronological data for the deposit, proposing a Paleoproterozoic (Rb-Sr in muscovite 1929 ± 17 Ma; 1946 ± 24 Pb-Pb in arsenopyrite) age for mineralization. We present here new insights from

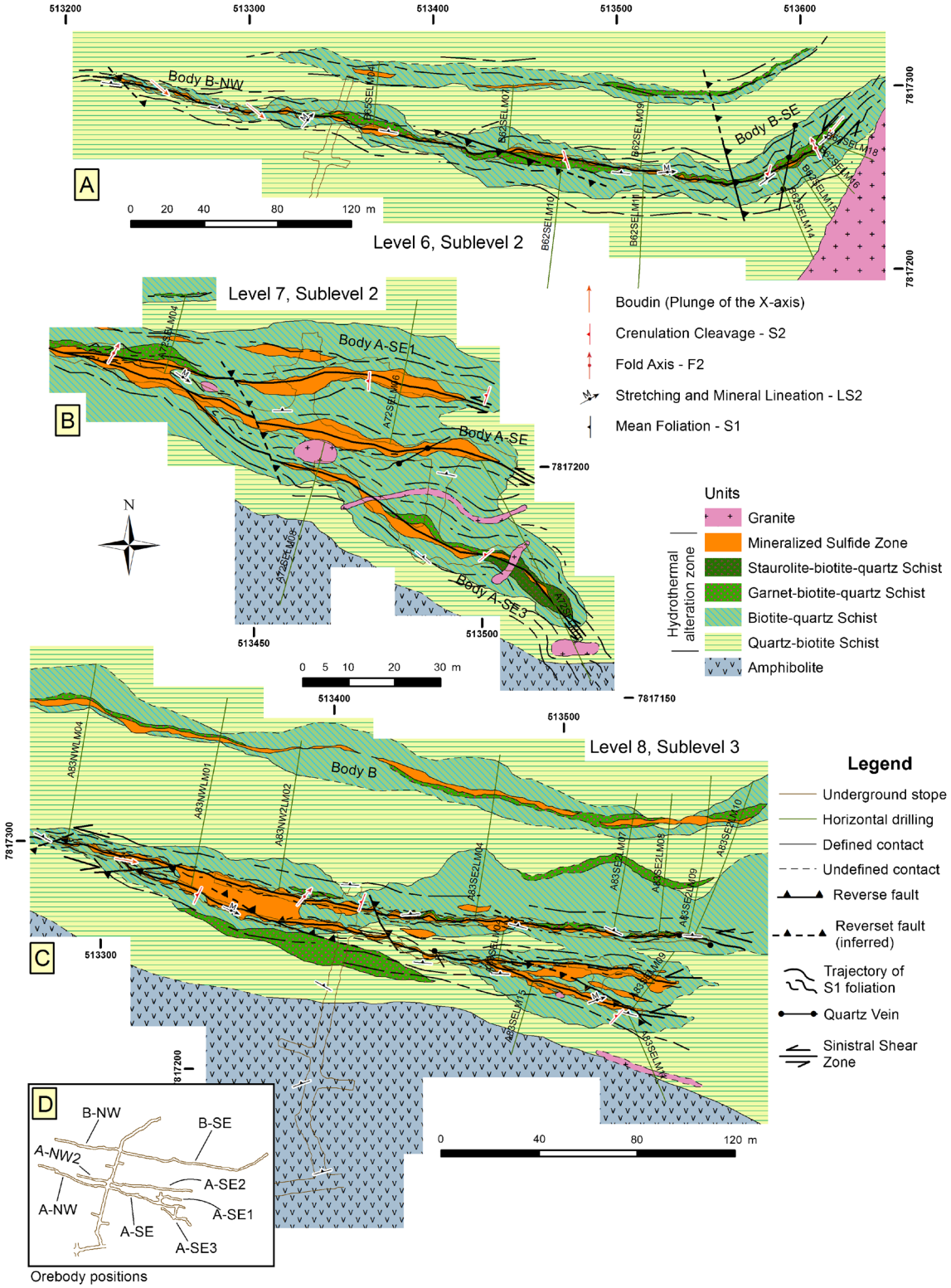

Fig. 2 Geological maps of the Turmalina deposit showing three underground levels of orebodies A and B. **a** Level 6, sublevel 2, elevation of 226 m. **b** Level 7, sublevel 2, elevation of 159 m. **c** Level 8, sublevel 3, elevation of 97 m. **d** Relative position of the underground stopes and orebodies in level 6, sublevel 2

underground mapping and sampling at the scales of 1:100 and 1:200 and from petrographic and microstructural studies, stratigraphic definition, structural analysis, mineral chemistry, thermometry, and sulfur isotope analysis.

Regional geological setting

The northwest of the QF is subdivided into the following (Renger et al. 1994; Alkmim and Marshak 1998; Romano 2006): (i) granite-gneiss complex, which corresponds to the crystalline basement; (ii) Archean greenstone belt, represented by the Rio das Velhas Supergroup or related sequence; and (iii) Proterozoic meta-sedimentary units, represented by the Minas Supergroup and Bambuí Group.

The domes of granite-gneiss complex are comprised of tonalite–trondhjemite–granodiorite (TTG) associations with interleaved amphibolites and meta-sedimentary rocks (Schorscher 1978; Ladeira 1980). The TTG associations represent the oldest Archean units of the QF, with a minimum age of 2.9 Ga (Machado et al. 1989; Machado and Carneiro 1992).

The Rio das Velhas Supergroup (Schorscher 1978) is an Archean sequence of meta-volcano-sedimentary rocks aged between 3.0 and 2.7 Ga (Machado and Carneiro 1992; Noce et al. 1998). This supergroup is divided into two groups, the basal Nova Lima Group succeeded by the Maquiné Group. The Nova Lima Group is composed of ultramafic and basaltic lavas, greywackes, and sandstones with interbedded BIFs, conglomerates, and carbonaceous pelites (Dorr 1957, 1969; Baltazar and Zucchetti 2007). The Maquiné Group contains sandstones, quartz pelites, and conglomerates. The lower contact of the Nova Lima Group with the TTG complex is usually igneous or tectonic.

Romano (2006) further subdivides the Nova Lima Group (Fig. 1b), in the NW area, from bottom to top, into the following: (i) meta-igneous and meta-sedimentary sequences of mafic-ultramafic volcanic rocks, and intercalations of meta-sedimentary rocks such as chert, phyllite, carbonaceous, and silicified layers, and (ii) meta-volcano-sedimentary and meta-sedimentary sequence, with pyroclastic rocks, tuffs, thin layers of BIF, greywackes, turbidites, and quartzites. In addition to these units, a series of 2.7 and 2.5 Ga granitoid intrusions are exposed along the Pitangui lineament (Romano 2006). The bodies are syn- to late-tectonic, coarse-grained biotite granites (Heineck 1997), referred to as the Mato Dentro Intrusive Suite, and display a geochemical signature of a continental collision environment (Romano et al. 1995).

The geological units of the QF display a pattern of superposed folds bounded by synclinal and anticlinal megastructures, commonly truncated by thrust faults (ESM Table 1; Alkmim and Marshak 1998; Baltazar and Zucchetti 2007). In the NW area, Romano (1989, 2006) interpreted a polyphase evolution in three distinctive events (ESM Table 1): (i) ductile Archean deformation (D_n), (ii) ductile-brittle Archean to Paleoproterozoic deformation (D_{n+1}), and (iii) late extensional tectonics representing the Brasiliano event. This author argued that events (i) and (ii) are regionally characterized by an axial planar foliation of kilometer-scale folds of undefined vergence, developed during the D_n event, which was superimposed by a mylonitic D_{n+1} foliation.

Methodology

The underground stopes were mapped at scales 1:200 and 1:100, identifying the geometric and structural characteristics of orebodies A and B at three mine levels, namely (i) level 8, sublevel 3 (orebody A); (ii) level 7, sublevel 2 (orebody A, SE sector); and (iii) level 6, sublevel 2 (orebody B). The following levels were mapped in less detail for correlation and sample collection: level 8, sublevel 4; level 7, sublevel 0; and level 6, sublevel 1. Mapping and sample collection were also based on the description of 25 horizontal underground diamond drill cores. Thirty-eight thin sections were made from samples collected during underground mapping and 15 from diamond drill cores for petrographic and structural description.

The microprobe analyses that focused on the mineralogical characterization of the mineralized zones and the sulfide compositions were performed at the Geoscience Institute of the University of Brasilia using a JEOL JXA-8230 microprobe. The sulfides were manually separated and mounted in 19 epoxy discs 24.4 mm in diameter and then polished. Garnet and biotite microprobe analyses were performed at the Microscopy Center of the Federal University of Minas Gerais with a JEOL JXA-8900RL microprobe. Both microprobes use four wavelength-dispersive spectrometers. The standard operating conditions were 15 kV accelerating voltage for silicates and 20 kV for sulfides, with a 25 nA beam current.

The 19 mounts of sulfide minerals were used for sulfide isotope analysis with a multi-collector mass spectrometer (LA-MC-ICP-MS Finnigan Neptune), coupled to a 213-μm New Wave solid-state laser at the Laboratory of Geochronology of the University of Brasilia. The sulfides (pyrite, pyrrhotite, chalcopyrite, and arsenopyrite) were analyzed after previous electron microprobe identification. The isotopes ^{34}S and ^{32}S were analyzed against the international standard IAEA-S1, and accuracy was monitored during the analytical sessions with the international standard IAEA-S3. The results are reported as $\delta^{34}S$ values relative to V-CDT, with errors given as 1 sigma standard deviations. Signals were taken in 40 cycles of about 1 s each in medium resolution mode of the ICP-MS. The laser spot size was 100 μm, with 90% laser intensity at 10 Hz and an energy level of 4–5 J/cm^2 on the sample surface. The analytical protocol is detailed in Bühn et al. (2012).

Lithostratigraphy, petrography, and metamorphism

Based on the proposal of Romano (2006), we subdivide the lithostratigraphic sequences into the following units: (i) basal

mafic-ultramafic unit, comprised of meta-volcanic basic rocks, serpentinites, and amphibole-mica schists; (ii) volcano-sedimentary unit, comprised of pyroclastic rocks and tuffs; (iii) clastic-chemical-sedimentary unit, consisting of carbonate layers, cherts, and BIFs; and (iv) clastic-sedimentary unit at the top, consisting of phyllite, quartzite, and volcano-clastic intervals.

The stratigraphy of the Turmalina deposit (ESM Fig. 1) also includes ortho-magmatic amphibolites of the mafic-ultramafic unit followed by a hydrothermally altered volcano-sedimentary sequence of tuffs and interspersed rhythmic pelitic rocks belonging to the volcano-sedimentary unit. A discordant granite stock with several apophyses in the SE area is a member of the Mato Dentro Intrusive Suite.

Mafic-ultramafic unit

The mafic-ultramafic unit is comprised of a dark green to gray, fine-grained ortho-amphibolite with a nematoblastic fabric defined by millimetric bands of hornblende (ESM Fig. 2b and c), minor actinolite, and chlorite, with a minimum thickness of 110 m. These rocks are widely exposed in the southern domain (Fig. 2b, c). The representative modal composition is Mg hornblende (60–80 vol.%), plagioclase (15 vol.%), chlorite (6 to 10 vol.%), quartz (2 to 10 vol.%), titanite (1 to 4 vol.%), and augite (< 3 vol.%) with some carbonate, sericite, garnet, biotite, ilmenite, and apatite. Augite is commonly altered to hornblende, and chlorite is an alteration product of plagioclase, hornblende, and garnet. The titanite often replaces ilmenite.

Volcano-sedimentary unit

The volcano-sedimentary unit is composed of a 180-m-thick package of interlayered meta-pelites and meta-tuffs. The rocks are fine-grained, dark gray colored and display a well-developed schistosity. Four varieties of schists were described that consist predominantly of biotite and quartz with a granolepidoblastic texture: (i) quartz-biotite schist, (ii) biotite-quartz schist, (iii) garnet-biotite-quartz schist, and (iv) staurolite-biotite-quartz schist. The lower contact of the volcano-sedimentary unit with the mafic-ultramafic unit is gradational.

In addition to biotite (siderophyllite and eastonite), quartz, garnet (almandine), and staurolite, these schists are formed by chlorite (10 to 30 vol.%, replacing biotite; ESM Fig. 2d), plagioclase (< 10 vol.%), carbonate, tourmaline (dravite), and zircon. Muscovite, amphibole (grunerite and cummingtonite), berthierite, ilmenite, titanite, epidote, hematite, and apatite are subordinate. Garnet-biotite-quartz schist (ESM Fig. 2h) and staurolite-biotite-quartz schists (ESM Fig. 2I) are restricted close to the orebodies. They contain 5 to 20 vol.% garnet and 5 to 15 vol.% staurolite, which is observed as light yellow idioblasts of about 1 cm in length containing abundant quartz inclusions. The staurolite may be completely replaced by chlorite.

Granite–Mato Dentro Intrusive Suite

A granite stock is exposed throughout the eastern portion of the Turmalina deposit in a NNE-SSW-trending contact with the meta-volcano-sedimentary sequence (Fig. 2a). The rock is coarse grained (ESM Fig. 2f) and composed of quartz (35 to 50 vol.%), saussuritized plagioclase (20 to 25 vol.%), and K feldspar (10 to 20 vol.%) with corroded rims and locally chloritized biotite (10 to 25 vol.%). Muscovite, zircon, and titanite are subordinate. A series of granite apophyses (Fig. 2b, ESM Fig. 2g) with a thickness of 1–3 m can be observed in the SE area of the deposit. They are slightly richer in biotite and poorer in plagioclase than the granite stock.

Metamorphism

The metamorphic assemblage of the volcano-sedimentary unit is comprised of quartz-biotite-garnet-staurolite-plagioclase-andesine-ilmenite ± titanite. In the mafic-ultramafic unit, the metamorphic assemblage is made up of hornblende-plagioclase-quartz-garnet-ilmenite-titanite, where hornblende replaced igneous pyroxene (augite). Both assemblages indicate low to medium amphibolite grade metamorphism (Bucher and Grapes 2011). Biotite and staurolite are commonly altered to metamorphic chlorite, indicating retrograde metamorphism.

Deformation events and structural control of mineralization

The Turmalina deposit is controlled by a WNW-ESE-trending and steeply NNE-dipping shear zone which can be subdivided into four structural domains: N, NE, SW, and SE (Fig. 3). In the N domain, orebody B generally trends N080, whereas in the NE, this orebody is flexed and the shear zone turns from WNW-ESE to NE-SW-striking with a 67°–70° dip to the NW. In the SW and SE domains, orebody A has sub-orebodies that show a horsetail geometry termination and present directions varying between N070°W and E-W. The areas of intersection between sub-orebodies usually show an increase of the gold grade by 20 to 30%. The largest of these shear zone intersections is located between the body A-NW and A-NW2 (SW domain of Figs. 2c and 3). This area is an important exploration target, which can locally reach the average grade of 9–15 g/t/Au (obtained from drill cores). Detailed mapping and structural analysis indicate a structural evolution during three deformation events: D_1, D_2, and D_3.

The first deformation event (D_1), developed during an early stage of shortening, includes a regional isoclinal fold (F_1) and its penetrative axial-planar foliation (S_1). A compositional and

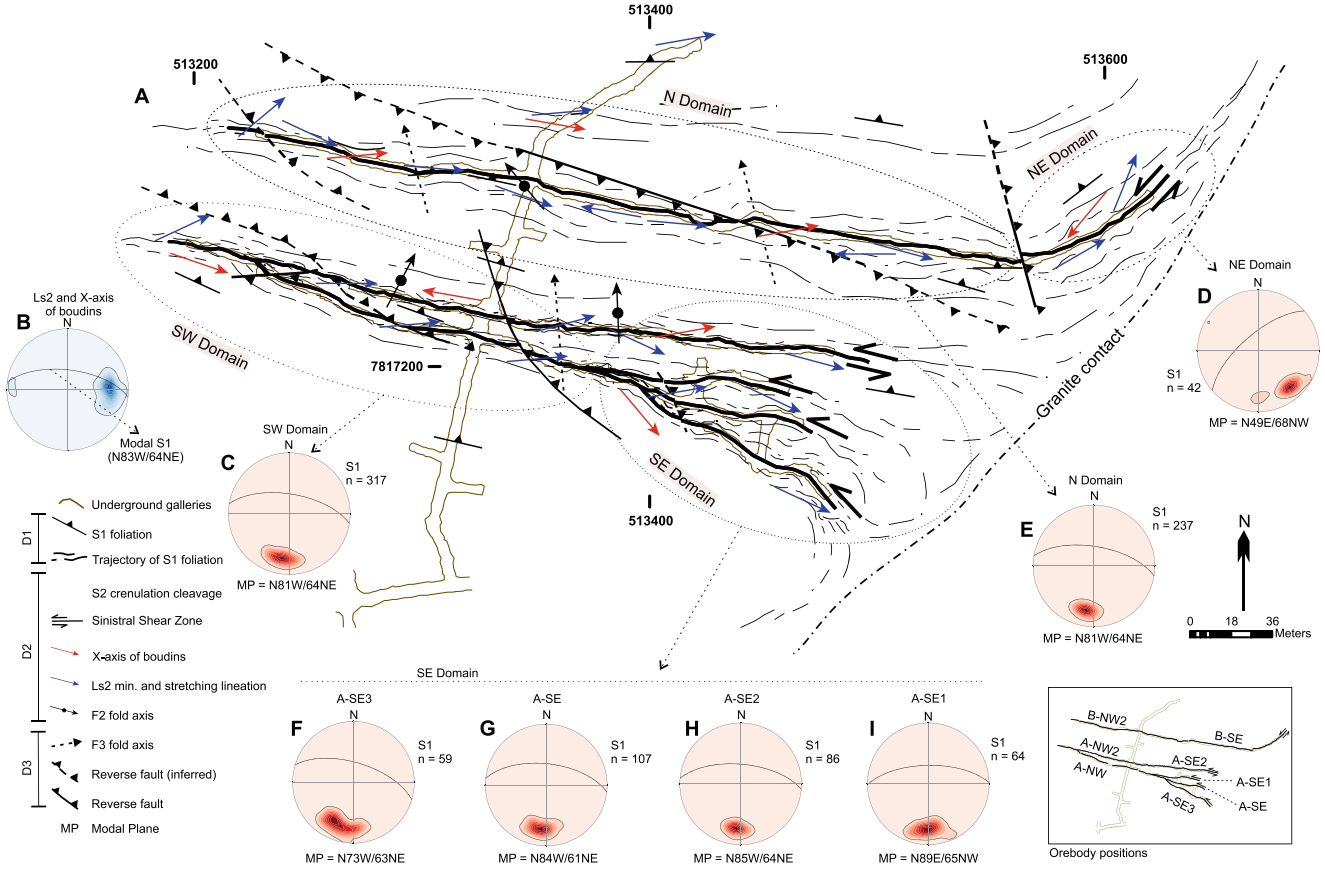

Fig. 3 **a** Detailed map and structural analysis of level 8, sublevel 3 at the Turmalina deposit showing shear zones. The *X*-axis of boudins (red narrows) and mineral and stretching lineation Ls_2 (blue narrows) relate to the D_2 deformation event, and the reverse faults relate to the D_3 deformation event. Note the representative position of orebodies in the inset map. **b** Stereographic projection (lower hemisphere, equal area projection) of the Ls_2 lineation associated with the S_1 cleavage plane. Contours are 2%. **c**–**i** Stereographic projections (lower hemisphere, equal projection area) of S_1 in the domains SW, N, NE, and SE, respectively. Contours are 5%

gradational banding is overprinted by the main foliation (S_1), which is expressed by the orientation of biotite and chlorite, locally of sericite, and by thin layers (< 5 mm) of fine (10 μm) quartz. The orientation of S_1 is relatively constant, with a direction close to N080°W and NNE dipping (with a mean of N083°W/64NE; Fig. 4b).

The second deformation event (D_2) is represented by the following: (i) ductile shear zones, (ii) mineral and stretching lineation (Ls_2), (iii) boudins and pinch-and-swell-type structures in quartz veins, (iv) crenulation cleavage (S_2), (v) crenulation lineation (L_2), and (vi) tight F_2 folds. The Ls_2 is represented by the orientation of mainly biotite and chlorite and elongated quartz grains. With moderate to shallow plunge towards the E (mean orientation 30/095), Ls_2 is well developed within the shear zones, especially in the N domain of the deposit, where it can be observed on S_1 planes. The crenulation cleavage S_2, which is also defined by planar fabric formed by biotite and chlorite, strikes from NNW-SSE to NNE-SSW, with a 65°–78° dip to the W (Fig. 4e–g). The S_2 is better developed in the intersection areas of orebody A, as a local fabric within the shear zone splays, where it is axial planar to the locally developed tight F_2 folds (Fig. 4h). The L_2 crenulation axes are approximately perpendicular to Ls_2, plunging 54°–64° towards 280°–317°, with an average of 62/299 (Fig. 4c). The axes of F_2 folds plunge 50°–75° with a NW-SE to NE-SW trend. The orientation of asymmetric boudins, mica fish, and S-C fabrics indicates a general sinistral sense of movement (ESM Fig. 3).

The D_3 event affects all rocks of the deposit and is represented by F_3 folds and two populations of reverse faults. The F_3 folds are open to tight, meter scale, with axis plunging to the NW (mean 65/325) and an axial plane dipping 60°–70° to the NE. These folds are observed throughout the deposit but are more abundant close to the orebodies. Reverse faults are ubiquitous in the Turmalina deposit and can be divided into two populations. The first (Fig. 4i) strikes ESE-WNW dipping 50°–55° mostly to the north, but locally also to the south of the orebody (showing a set of conjugate faults). In the horizontal plane, the traces of these faults commonly intercept the shear zones at an oblique angle of 10°–45°. The second population of faults (Fig. 4j) cross-cuts the first population and trends NW-SE, with an average dip of 30° to the NE. The

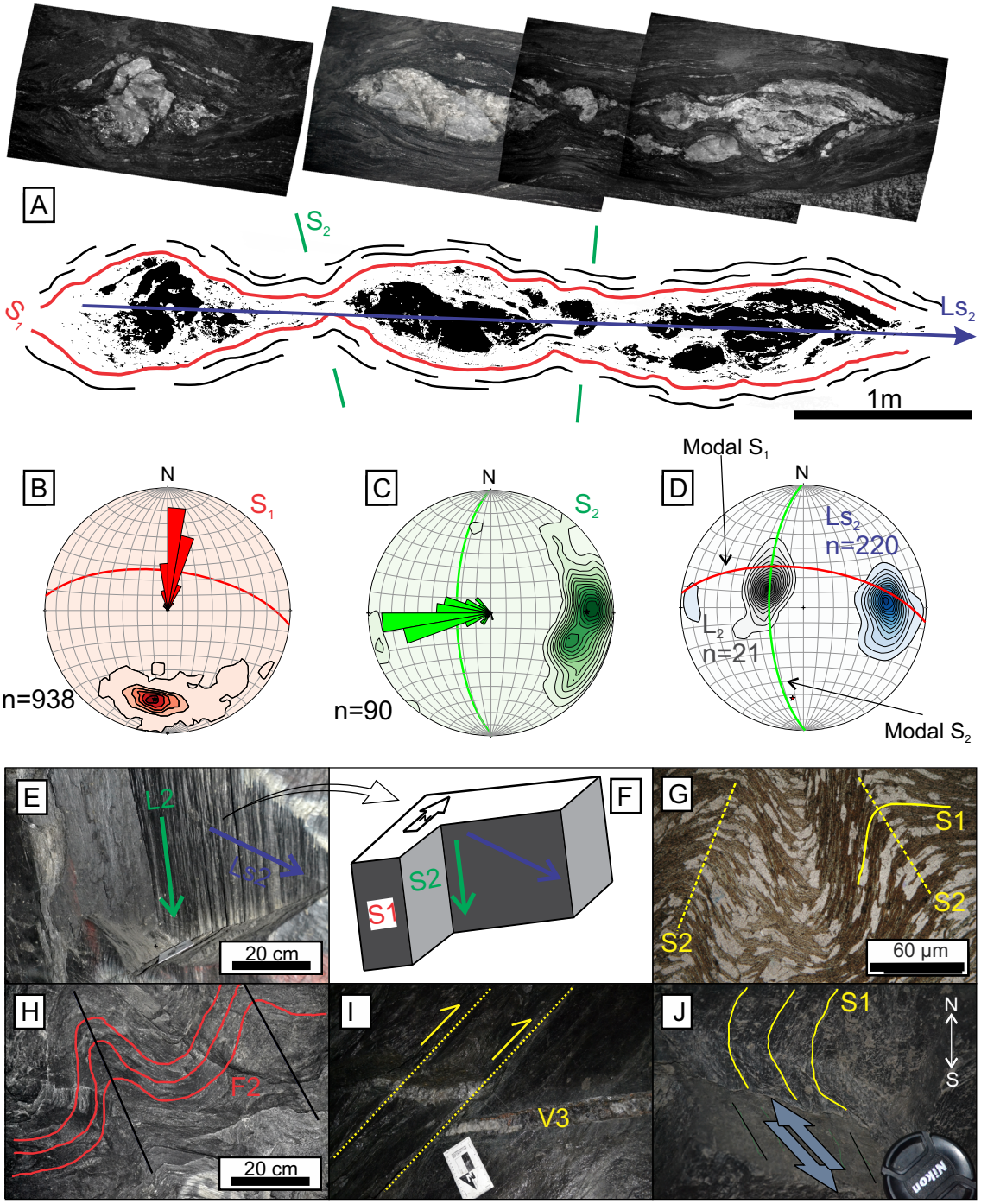

Fig. 4 **a** Typical structure of V_{1-2} quartz veins showing the S_1 foliation, the stretching lineation Ls_2 and boudins (the arrow indicates the dip direction of the boudin *X*-axis), and the crenulation cleavage S_2. Level 7, sublevel 2 of orebody A-SE. **b** Stereographic projection and rose diagram of S_1 foliation measurements throughout the deposit except for the NE domain, orebody B. Contours are 4%. The rose diagram indicates a maximum of 34%. **c** Stereographic projection and rose diagram of S_2 foliation throughout the deposit. Contours are 2%. The rose diagram indicates a maximum of 34% per 10°. **d** Stereographic projection of lineations Ls_2 and L_2 and the modal values of S_1 and S_2 planes. Contours for lineations are 2%. All projections are equal area projections of the lower hemisphere. **e**, **f** General aspect of S_1 and S_2 cleavage planes and Ls_2 and L_2 lineations in outcrop-scale hanging wall of orebody A-NW at level 8, sublevel 3. **g** Photomicrograph of quartz-biotite schist showing well-developed S_2 cleavage planes. **h** F_2 tight fold. **i** First population of reverse faults with vergence towards the SW, and V_3 vein. **j** Second population reverse fault with a dip towards the SSE showing a flexure of the S_1 foliation and slickensides developed on the fault plane

displacement of the two fault populations ranges from a few centimeters to about 6 m.

The growth of the three garnet porphyroblasts

Three garnet generations (Grt_1, Grt_2, and Grt_3) are present in the Turmalina deposit. The Grt_1 and Grt_2 occur as aggregates in decimetric bands parallel to the S_1 foliation. These bands commonly occur as a guide for the mineralized zone, delimiting it at the base and at the top.

Grt_1 occurs as idiomorphic and poikiloblastic crystals of up to 3 cm in diameter with inclusions of biotite, quartz, ilmenite, and sulfides adjacent to the orebodies. The blasts display pressure shadows and an internal foliation (S_i) with two textural patterns of inclusions: spiral trail and straight trail. At the garnet rims, inclusions are less common and are parallel to the external foliation (S_1).

Garnet Grt_2 occurs as overgrowth of Grt_1 or as scattered crystals with an average size of 0.5 cm. They are also idioblasts and contain only a few inclusions of biotite, quartz, and sulfides (mainly pyrrhotite and arsenopyrite). Some porphyroblasts have cores with helicitic inclusions, but less frequent than the Grt_1. Most Grt_2 show neither inclusions nor pressure shadows nor deflection of the foliation around the blasts.

The garnet Grt_3 is observed throughout the volcano-sedimentary sequence, but especially close to the orebodies. The garnet porphyroblasts of this generation have a size of only about 200 μm, overgrowing the structural fabric. They are nearly free of inclusions and rarely show alteration to chlorite.

Garnet compositions and garnet-biotite geothermometer

Growth zoning can be obliterated in high metamorphic grade garnets through volume diffusion, which exhibit zoning patterns that are reversed from those resulting from growth zoning (Yardley 1977). Some characteristics of garnets that have diffusional zonation include an increased Mn (from core to rim), a decreased Mg content, and a flat Ca profile (Tuccillo et al. 1990), as is commonly found in zoned high-grade metamorphic garnets. In Turmalina, garnet chemical profile studies (ESM Fig. 4; ESM Table 2) indicate the possibility of the diffusional zonation, especially in the Mn-rich rim Grt_1, whereas the analyses from the Grt_2 show preserved growth zonation pattern, which is consistent with the advocated models of garnet growth during prograde metamorphism. This kind of condition was documented by Petrakakis (1986), Tuccillo et al. (1990), and Cooke et al. (2000) among others, which presented Ca- and Mn-rich relict cores that attained peak temperatures higher than 650 °C.

Electron microprobe analyses of Grt_1 show a distinct compositional zonation of this mineral (ESM Fig. 4a and b; ESM Table 2) with an increase of CaO and MnO and a decrease of MgO from core to rim. The inclusion-rich cores show an increase of spessartine (from ~ 3 to 12 vol.% at the rim) and grossular (from ~ 5 to 17 vol.%) and a considerable decrease of pyrope content from core to rim. Garnet Grt_2 presents less strong compositional zoning, but all profiles suggest a decrease of CaO and MnO and an increase of FeO and MgO from core to rim (ESM Fig. 4a and c; ESM Table 2). Garnet Grt_3 shows only minor zoning and is significantly richer in MnO and poorer in MgO and CaO than Grt_1 and Grt_2 (ESM Fig. 4e; ESM Table 2).

Analyses of garnet porphyroblasts in equilibrium with biotite were observed in different samples of the schists. Garnets were analyzed along profiles, whereas biotites were analyzed in core and rim. Equilibrium temperatures were estimated using the thermodynamic database TWQ (version 2.10; Berman 1991), considering the exchange reaction of Fe-Mg: $Fe_3Al_2Si_3O_{12} + KMg_3Si_3AlO_{10}(OH)_2 \rightarrow Mg_3Al_2Si_3O_{12} + KFe_3Si_3AlO_{10}(OH)_2$. Ten Grt-Bt pairs of different garnet generations were analyzed (ESM Table 3). The absence of biotite inclusions in the Grt_2 and Grt_3 grains prevented the calculation of equilibrium temperatures for the garnet cores.

Applying a pressure estimate of 3–4 kbar (Tassinari et al. 2015), the highest metamorphic temperatures (ESM Fig. 4f) were recorded for Grt_2 rims (627 to 633 °C) and the lowest for the Grt_3 rims (~ 518 to 537 °C). Even acknowledging that Grt_1 may have undergone an additional diffusional resetting during cooling, the temperatures calculated for Grt_1 suggest a temperature decrease from core to the garnet rim (~ 592 to 625 °C towards ~ 548 to 600 °C, respectively). Caddick et al. (2010) postulate that to preserve initial core compositions, garnet crystals that experience amphibolite grade conditions should be at least 5 mm in diameter (in this case, Grt_1 can easily reach 30 mm) and subjected to minimal heating during exhumation.

Hydrothermal alteration

Several processes of hydrothermal alteration affect the rocks of the Turmalina deposit in association with a mineralized envelope. We summarize at least six hydrothermal alteration processes including silicification, chloritization, sericitization, carbonatization, tourmalinization, and sulfidation.

Silicification is the dominant process of alteration with the development of fine, recrystallized granoblastic quartz in the host rocks and the presence of smoky and milky quartz veins, most of the times subparallel to the S_1 foliation. The silicification is associated with pyrrhotite, arsenopyrite, and pyrite with minor amounts of chalcopyrite and löllingite, which are

commonly disseminated as bands or at the edges of the quartz veins. Carbonate appears mainly together with quartz either as veinlets, concordant, or discordant to S_1 or in the interstices between quartz grains. Sericite replaces almost completely the metamorphic plagioclase from the volcano-sedimentary sequence, and widely distributed chlorite is late to post sulfidation (some crystals overlap sulfides). Hydrothermal chlorite is located in centimeter-thick bands parallel to S_1, more frequent in the proximal alteration zone (see below), where very fine granulation occurs with preserved pleochroism of the biotite.

Vein system and quartz textures

The Turmalina deposit contains three generations of veins ($V_{1–2}$, V_3, and V_4; Fig. 5) comprised by quartz (> 80 vol.%), carbonate (5 to 20 vol.%), and subordinate feldspar and sulfides with the local development of boudins and hydraulic breccias. In this study, we focus on quartz veins closely associated with shear zones at the boundaries of the ore zone ($V_{1–2}$ and V_3).

The $V_{1–2}$ vein is related to the D_1 and D_2 deformation events and is the main vein associated with gold mineralization, which occurs as boudins, pinch-and-swell lenses, and locally hydraulic breccias. These veins range from millimeters to meters in thickness (usually 1 m or less although they may reach up to 3 m). They consist of coarse- to medium-grained, smoky and milky quartz with a minor amount of carbonate, feldspar, sulfides, and gold and are parallel to the main foliation (S_1) (Fig. 4a). In hand specimen, they contain irregular grain boundaries (Fig. 5a). The granoblastic quartz displays variable degrees of recrystallization and shearing. In general, quartz with moderate subgrain development and undulose extinction is restricted to the shear zones, whereas quartz with deformation lamellae is widespread, indicating that ductile deformation and dynamic recrystallization had variable intensity during the development of D_2 deformation event.

The $V_{1–2}$ vein minerals have two phases of formation. The first phase is characterized by milky quartz and small amounts of feldspar and is volumetrically dominant (milky quartz represents about 70 vol.% of total quartz in $V_{1–2}$ veins). The second phase of the $V_{1–2}$ vein is defined by the deformation of milky quartz and the precipitation of smoky quartz, sulfides, and gold. These silicate and carbonate minerals are interpreted to have formed synchronously with pyrrhotite-arsenopyrite ± löllingite ± chalcopyrite sulfide assemblage.

The V_3 vein type (Fig. 5c, d) is composed of granular milky and smoky quartz containing sulfide (5 to 15 vol.%) and minor gold. Their thickness may reach 30 cm, and they are found along the reverse faults, where they usually contain coarse-grained (< 2 cm), euhedral to subhedral milky quartz and

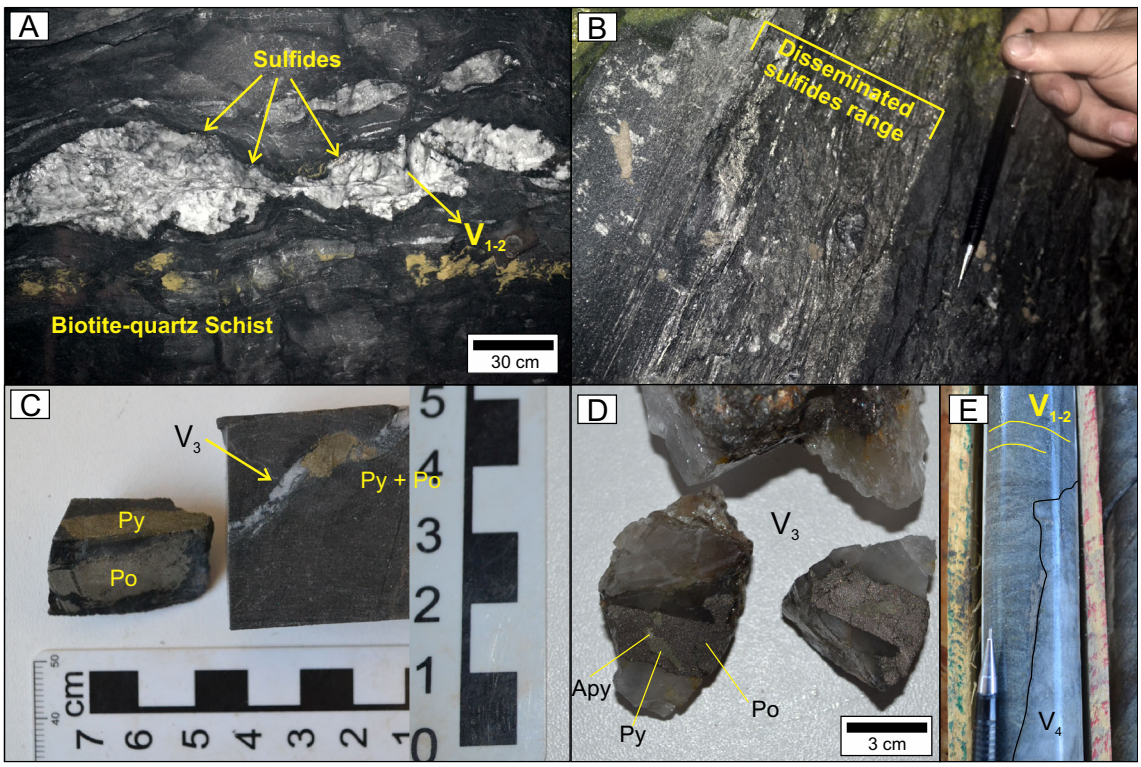

Fig. 5 Vein types and mineralization styles. **a** Boudin-aged $V_{1–2}$ vein on the ceiling of the underground stope. Orebody A-SE2. **b** Band of disseminated sulfides. View to SE, end of the stope in development. Orebody A-SE. **c** Drill core B62SELM10 showing V_3 vein with pyrite and pyrrhotite. **d** V_3 vein with pyrrhotite, pyrite, and arsenopyrite. **e** Drill core A72SELM10 with V_4 quartz vein, discordant to S_1, with pyrite at the border. Apy arsenopyrite, Po pyrrhotite, Py pyrite

carbonate grains, which define mineral growth fibers that are perpendicular to vein margins. On a microscopic scale, they also occur as veinlets orthogonal to S_1, where they are abundant (> 15 vol.%) in carbonate (mainly ankerite, less calcite).

The barren V_4 quartz veins with various textures and orientations, from en echelon steep to flat-lying veins, cross-cut all structures. The V_4 veins are composed of milky quartz and have a thickness of up to 20 cm (Fig. 5e). Pyrite is the dominant sulfide (> 5 vol.% of the veins), which is devoid of mineral inclusions and displays a smooth surface. Pyrite and pyrrhotite (Fig. 6f) occur as scattered aggregates of euhedral to subhedral, fine- to medium-grained (< 3 mm) crystals.

Hydrothermal alteration zones

The four main hydrothermal alteration zones distinguished in the volcano-sedimentary unit (Fig. 7) are as follows: (i) mineralized sulfide zone (main lodes) with the quartz-sulfide ± tourmaline ± carbonate assemblage; (ii) proximal quartz-chlorite-sericite-sulfide ± carbonate ± tourmaline that displays the highest gold grade, especially adjacent to the $V_{1–2}$ quartz veins; (iii) intermediate quartz-chlorite ± sericite ± carbonate; and (iv) distal (further away from $V_{1–2}$ veins) quartz-chlorite-carbonate ± sericite.

The boundaries among these zones are gradational over the decimeter to meter scales, and the spatial distribution of the hydrothermal phases throughout the alteration types is summarized in Table 1. The most conspicuous hydrothermal processes in the Turmalina deposit are, in general, the degree of quartz and chlorite enrichment, which increases from the distal towards the proximal zone. Although the mafic-ultramafic unit is variably altered, it does not host economically significant gold concentrations and is not discussed further.

The main lodes, represented by a mineralized sulfide zone (quartz-sulfide ± tourmaline ± carbonate; 3 to 7 m wide), are marked by a high abundance of dense quartz veins and high concentrations of sulfide minerals, besides tourmaline, carbonate, and rare grunerite.

The proximal quartz-chlorite-sericite-sulfide ± carbonate ± tourmaline alteration zone extends from the vein boundaries into the staurolite-biotite-quartz and garnet-biotite-quartz schists (Fig. 7; Table 1) and is characterized by preferential replacement of metamorphic garnet (Grt_1 and Grt_2)-biotite ± staurolite ± amphibole ± rutile ± apatite ± berthierite by hydrothermal chlorite, sericite, and less abundant carbonate, sulfide, rutile, monazite, ilmenite, and titanite. The width of the proximal alteration zone is proportional to the width of the $V_{1–2}$ quartz veins, rarely exceeding a few meters from these veins.

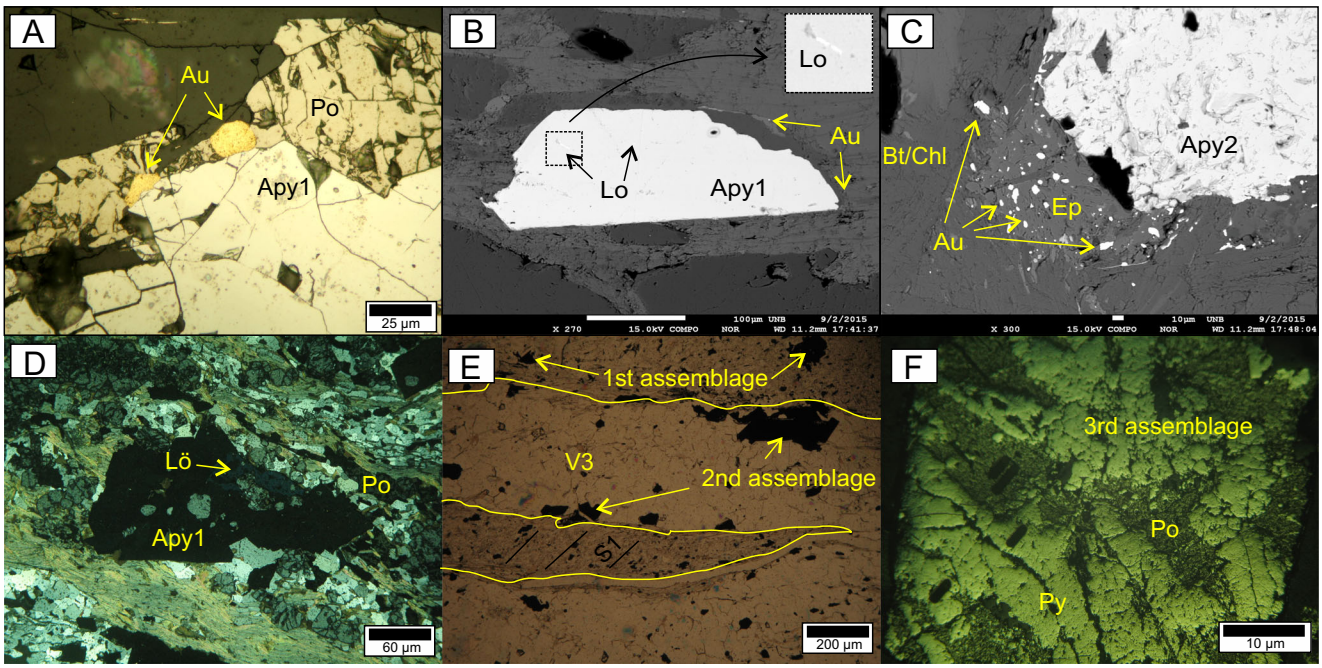

Fig. 6 Gold mineralization stages and sulfide assemblages of the Turmalina deposit. **a** Photomicrograph of gold grains in pyrrhotite in equilibrium with arsenopyrite from mineralization stage I (first sulfide assemblage). Parallel nichols, reflected light. **b** Back-scattered electron (BSE) image of an arsenopyrite crystal from mineralization stage I (first sulfide assemblage) with inclusion of löllingite and fine grains of gold on the border. **c** BSE image of arsenopyrite of the gold mineralization stage II (second sulfide assemblage) in equilibrium with epidote and disseminated gold grains. **d** Photomicrograph of typical mineralized sulfide zone with sulfides from po-apy ± lo assemblage, proximal alteration zone. This sulfide assemblage shows no retrograde gangue minerals, and arsenopyrite replaces löllingite. Parallel nichols, reflected light. **e** Photomicrograph of the first and second sulfide assemblages which shows a quartz-carbonate-sericite veinlet (V_3) cross-cutting the main foliation S_1. Parallel nichols, transmitted light. **f** Photomicrograph of pyrite-pyrrhotite of the third sulfide assemblage from the V_4 vein. Apy arsenopyrite, Po pyrrhotite, Lo löllingite, Py pyrite, Ep epidote, Au gold

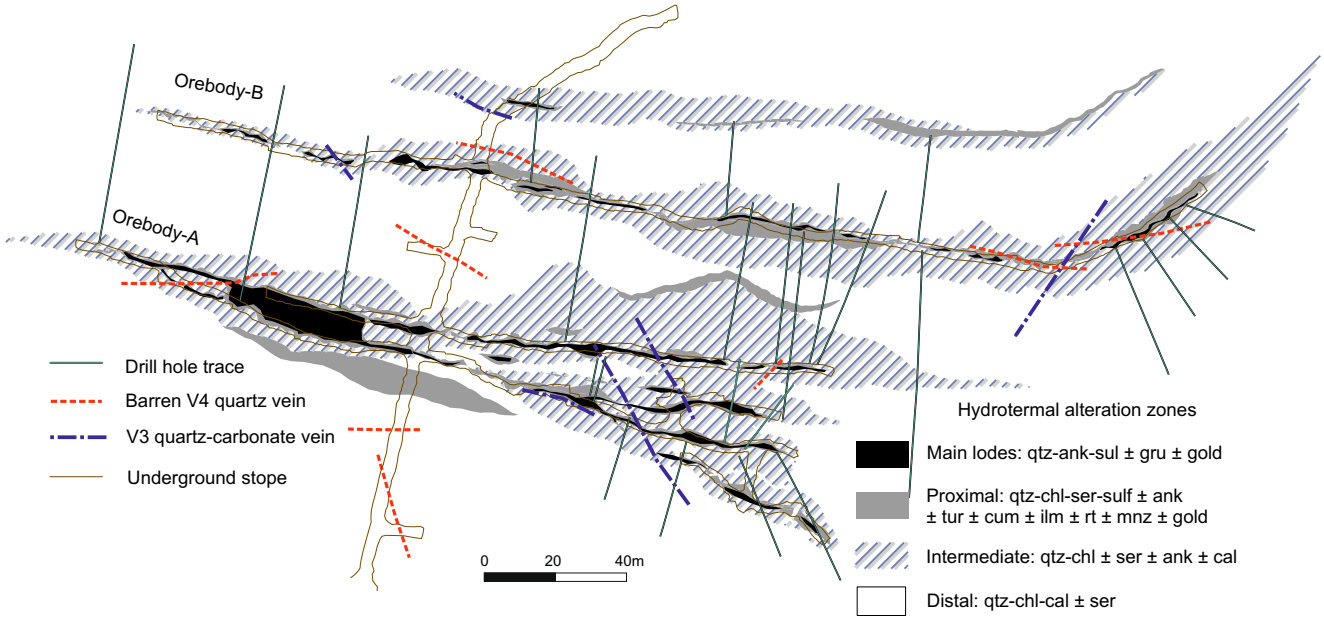

Fig. 7 Schematic plan view of the distribution of hydrothermal alteration zones to the volcano-sedimentary unit in the Turmalina deposit. The intensity of hydrothermal alteration increases with proximity to shear zones. ank ankerite, cal calcite, chl chlorite, cum cummingtonite, gru grunerite, ilm ilmenite, mnz monazite, qtz quartz, rt rutile, ser sericite, sul sulfide, tur tourmaline

The proximal zone is quartz-chlorite-sericite rich, with subordinated carbonate and tourmaline, cummingtonite, ilmenite, rutile, and monazite.

Fine-grained chlorite partially replaces biotite and garnet (mainly Grt_1; less frequently, Grt_2) and commonly completely replaces staurolite. Chlorite forms colorless to olive green crystals in the proximal zone, where very fine granulation occurs with preserved pleochroism of the biotite. In the interstices between porphyroblasts, chlorite forms an aggregate with rosette morphology. The quartz-chlorite-sericite

Table 1 Schematic geographic distribution of the hydrothermal alteration types in the Turmalina deposit

Primary phases	Hydrothermal alteration zones and assemblages				
	Quartz-biotite schist	Biotite-quartz schist	Garnet-biotite-quartz schist	Staurolite-garnet-biotite-quartz schist	Mineralized sulfide zone
	Distal zone	Intermediate zone	Proximal zone		Main lodes
	Quartz-chlorite-carbonate ± sericite	Quartz-chlorite ± sericite ± carbonate	Quartz-chlorite-sericite-sulfide ± carbonate ± tourmaline		Quartz-sulfide ± tourmaline ± carbonate
Biotite	Partly replaced by chlorite sericite and muscovite		Most times replaced by chlorite and carbonate (in V_3 veinlet)		
Staurolite	Absent		Completely replaced by chlorite and sericite	Unstable, partly replaced by chlorite and sericite	
Garnets Grt_1 and Grt_2	Absent		Unstable, partly replaced by sericite, quartz, sulfides, and iron oxides (?)		Rare, unstable
Apatite	Less common, replaced by rutile		Replaced by rutile and monazite		Absent
Feldspar	Unstable, partly replaced by sericite	Unstable, almost completely replaced by sericite or occasionally by epidote			
Quartz	Partly stable		Hydrothermal quartz more or less recrystallized		Hydrothermal quartz recrystallized
Rutile	Partly replaced by ilmenite and titanite				Absent
Amphibole	Stable cummingtonite (accessory)	Cummingtonite and grunerite, altered into sericite and chlorite			Rare, most grunerite
Total opaques	Accessory hematite and pyrite (< 1 vol.%)		Mainly sulfides (1–10 vol.%)		Mainly sulfides (5–15 vol.%)
Thickness (m)	> 50	15–40	2–5		3–7

alteration is cross-cut by a few < 1-cm-wide quartz-ankerite ± calcite veinlets (V_3). Euhedral to subhedral tourmaline (dravite) is located in fine-grained bands (ESM Fig. 2h), along with the margins of quartz veins composed mainly of quartz, garnet, and sulfides, and rarely exceeds 5 vol.% of the bands. Tourmaline grains display no chemical zoning or a core-and-rim texture.

The intermediate quartz-chlorite ± sericite ± carbonate alteration zone is located in a 15- to 40-m-wide parallel band within high-strain zones and is marked mainly by preferential replacement of biotite-plagioclase by chlorite-sericite-carbonate assemblage (Fig. 7; Table 1). This alteration zone displays chlorite-rich domains (2- to 15-cm-wide bands), which are concordant with S_1 and may contain very fine acicular muscovite ± hematite. Sericite is preferentially developed by replacement of plagioclase and may occur as strain shadows with quartz. Carbonate in the intermediate alteration zone appears mainly in the interstices between quartz grains. Rare "calcite eye bands" are defined by rounded clots of calcite. Sericite appears as fine-grained flakes, commonly associated with chlorite-rich domains.

The distal zone is characterized by an assemblage of quartz-chlorite-carbonate ± sericite with less abundant quartz and chlorite (from 60 to 35 vol.%) than in the intermediate zone (Fig. 7; Table 1). Carbonate minerals are more abundant in the distal zone and appear as calcite in interstices between quartz grains or partially replacing chlorite and biotite. Muscovite, sericite, and chlorite occur also as randomly to weakly oriented fine-grained flakes and aggregates associated with calcite.

Mineralization

Mineralization styles

Gold mineralization in Turmalina is associated with sulfides and can be divided into two styles: (i) disseminated, gold-bearing sulfide-quartz grains parallel to S_1 in bands that are 5 to 25 cm thick (Fig. 5b) [a large proportion (80 to 90 vol.%) of the gold-bearing sulfide grains are aligned with the S_1 foliation, but sulfides may also be found along spaced cleavage planes (S_2)] and (ii) gold in sulfide aggregates at the borders of the $V_{1–2}$ and V_3 quartz-feldspar ± carbonate ± sulfide veins (Fig. 5a). These aggregates are a few centimeters in diameter and are located at the interior or the border of the veins, especially in the "necks" of the pinch-and-swell structures.

The disseminated gold-bearing sulfide grains are the main style of mineralization. The gold is present in the crystal lattice of the sulfides and as native gold, where it appears as 10- to 60-μm small grains, with smooth surfaces and irregular shapes in equilibrium with arsenopyrite, or as inclusion in pyrrhotite, pyrite, epidote, or quartz, commonly bordering arsenopyrite (Fig. 6a–c).

The two stages of gold mineralization

The gold-bearing sulfides and oxide assemblages are defined by arsenopyrite-pyrrhotite ± pyrite ± chalcopyrite ± löllingite ± rutile ± ilmenite ± titanite ± galena ± hematite. Arsenopyrite replaces löllingite (Fig. 6d). Ilmenite and titanite generally replace rutile, which appears to be better preserved in the distal zones.

Two stages of gold mineralization are identified based on cross-cutting relationships, hydrothermal silicate-carbonate assemblages and sulfide-oxide mineralogy: an early sulfide-rich pyrrhotite-arsenopyrite ± löllingite ± chalcopyrite (gold mineralization stage I) and a later pyrrhotite-pyrite-arsenopyrite ± chalcopyrite (gold mineralization stage II). Gold-bearing veins, which contain quartz-sericite-sulfide (pyrrhotite-arsenopyrite ± löllingite ± chalcopyrite assemblage) stage I, are overprinted by quartz-chlorite-ankerite-sericite-sulfide (pyrrhotite-pyrite-arsenopyrite ± chalcopyrite assemblage)-tourmaline ± epidote ± calcite stage II (Fig. 6e).

Mineralization stage I

The pyrrhotite-arsenopyrite ± löllingite ± chalcopyrite assemblage from mineralization stage I represents at least 70 vol.% of the orebodies and is the main gold mineralization stage. This stage is defined by S_1 foliation-parallel, gold-bearing $V_{1–2}$ veins and pervasive wall rock alteration and occurs as fine crystals (< 30 μm) in polycrystalline aggregates or disseminated along foliation plane. Pyrrhotite accounts for 60 to 75 vol.% and is commonly in equilibrium with 10 to 30 vol.% of arsenopyrite, 2 to 4 vol.% of löllingite, and rare chalcopyrite. Pyrrhotite grains (10 to 60 μm) are commonly inclusion rich (mainly chalcopyrite and quartz) and fill fractures in chalcopyrite. The arsenopyrites are mostly present as fine-grained, subhedral, prismatic to acicular grains (50 to 130 μm). The abundance of arsenopyrite is typically higher in the bands of the disseminated gold-bearing sulfide style than in the gold sulfide aggregate style, where pyrrhotite is mostly the only sulfide.

Mineralization stage II

The gold mineralization pyrrhotite-pyrite-arsenopyrite ± chalcopyrite stage II is characterized mainly by S_1 foliation-discordant, quartz-carbonate V_3 veins/veinlets (Fig. 6e), as well as disseminated gold. The sulfides of the second assemblage are comprised of pyrrhotite (> 50 vol.% of sulfides) that commonly is located as aggregates of subhedral fine (< 30 μm) crystals, euhedral pyrite (30 to 40 vol.%), and euhedral to subhedral arsenopyrite crystals (< 10 vol.%) that grow up to

300 μm in size. Accessory chalcopyrite occurs as subhedral crystals enclosed in pyrite and arsenopyrite, crystals intergrown with pyrite, and interstitial space infill between pyrite crystals. Traces of galena are observed as infill in pyrite microfractures and are commonly associated with pyrrhotite and chalcopyrite. The sulfides from gold mineralization stage II are the result of the recrystallization of existing sulfides (stage I) or represent new grains hosted in the quartz-carbonate-sericite V_3 veins.

Arsenopyrite geothermometer

Geothermometric studies in arsenopyrite in equilibrium with löllingite, pyrrhotite, and gold were performed for stage I. For mineralization stage II, arsenopyrites in equilibrium with pyrrhotite, pyrite, and gold were used. The lack of chemical zoning, the observation of arsenopyrite in equilibrium with pyrrhotite-löllingite for the gold mineralization stage I and with pyrrhotite-pyrite for the gold mineralization stage II, and the low content (< 1 wt%) of combined minor elements allow for the use of the arsenopyrite geothermometer to constrain the temperature of mineralization, based on Kretschmar and Scott (1976) and Sharp et al. (1985).

The results (ESM Table 4) show values between 36.30 and 37.06 at.% As for mineralization stage I and 30.76 and 34.64 at.% As for mineralization stage II. These data, plotted in Fig. 8, suggest two significantly different temperatures for each assemblage. The samples, representing the arsenopyrite from the gold mineralization stage I, indicate temperatures between 542 ± 30 °C (AM-10_A) and 598 ± 19 °C (AM-71_A). The pyrrhotite-pyrite-arsenopyrite assemblage from the gold mineralization stage II, represented by samples AM65_C and AM82_A, suggests temperatures between 442 ± 9 and 510 ± 30 °C, respectively.

Sulfur isotopes

Twenty-one sulfide grains were sampled from disseminated sulfides and V_{1-2}, V_3, and V_4 quartz veins hosted in the

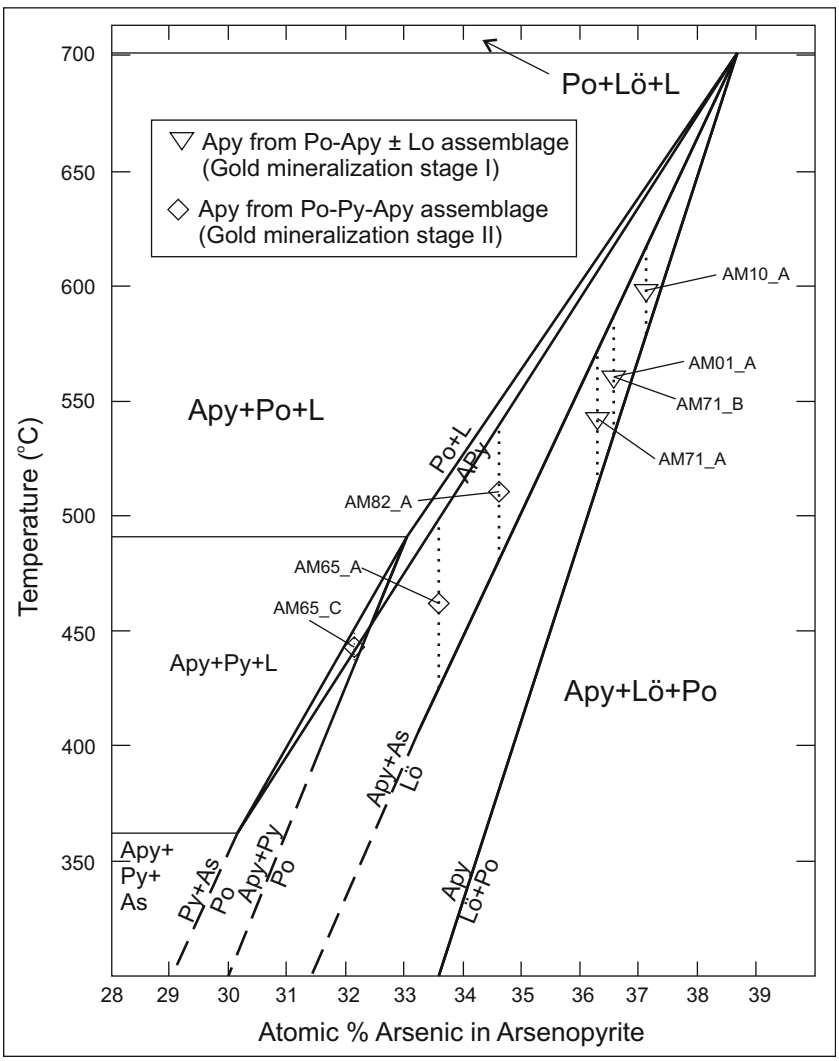

Fig. 8 Arsenopyrite geothermometer proposed by Kretschmar and Scott (1976), showing the composition of atomic percentage of arsenic in arsenopyrite as a function of equilibrium temperature. The Turmalina samples of the first sulfide assemblage (samples AM01, AM10, and AM71) are represented by the dark gray area, and the samples of the second sulfide assemblage are in light gray (AM65 and AM82)

volcano-sedimentary unit. Sulfide grains included up to 1-cm-wide, mineralization stage I pyrrhotite and arsenopyrite that are in equilibrium with quartz and gold, as well as mineralization stage II pyrrhotite, pyrite, and arsenopyrite grains, which are in equilibrium with quartz and gold. Nine sulfide grains (pyrite and pyrrhotite) from V_4 barren quartz veins were also analyzed. Sulfur isotope $\delta^{34}S$ data from the two gold mineralization stages and from the pyrite-pyrrhotite assemblage (V_4 veins) are listed in ESM Table 5.

Arsenopyrites and pyrrhotites from the gold mineralization stage I display a range of $\delta^{34}S$ values from 3.99 to 4.19‰ and from 3.29 to 3.64‰, respectively. From mineralization stage II, $\delta^{34}S$ values range from 3.29 to 3.94‰ in arsenopyrite, from 2.94 to 3.74‰ in pyrrhotite, and from 3.33 to 5.76‰ in pyrite. The pyrite and pyrrhotite from barren V_4 quartz veins have $\delta^{34}S$ values ranging from 3.48 to 3.58‰ and from 3.56 to 4.41‰, respectively, very similar to the sulfides of mineralization stage I.

Discussion

The thermostructural evolution based on garnet generations

Three garnet generations were identified according to the following: (i) compositional zoning, (ii) microstructural zoning relative to the development of the S_1 and S_2 foliations, and (iii) their size. The timing of garnet growth relative to the deformation events and the gold mineralization stages is illustrated in Fig. 9.

Garnet Grt_1 has inclusion trails with orientations that reflect (in different blasts within the same sample or even in the same thin section) evolutionary stages of the S_1 foliation. Some porphyroblasts display a straight trail of inclusions in the core (internal foliation S_i) not parallel with the external foliation ($S_e = S_1$) that likely represent an early, pre- to syn-deformation stage of S_1 (Fig. 9a). Many Grt_1 porphyroblasts, however, show in their core a spiral trail of inclusions, which suggest garnet rotation during the evolution of the shear zone (Figs. 6a, b and 9b). Nevertheless, the complex pattern of inclusion trails did not allow determination of the sense of shear movement and S_1 rotation.

Electron microprobe profiles of Grt_1 crystals display a distinct compositional zoning that suggests growth under retrograde metamorphism (garnet-biotite geothermometry indicates temperatures of 592 to 625 °C for the core and 548 to 600 °C for the Grt_1 rims). Nevertheless, the mineral chemistry of Grt_1 indicates the possibility of diffusional zoning and, therefore, the obtained geothermometric data should be considered with caution. However, the obtained temperature values show consistency with the staurolite-garnet-biotite paragenesis (Bucher and Grapes 2011), and the size of the garnet porphyroblasts (up to 30 mm in diameter) favors the preservation of the core composition (cf. Caddick et al. 2010). These Grt_1 temperatures are also similar to the temperatures obtained from the arsenopyrite geothermometer of the pyrrhotite-arsenopyrite ± löllingite ± chalcopyrite assemblage from mineralization stage I (which also occurs as inclusions in Grt_1 and Grt_2).

Grt_2 garnets, in many places, overgrow Grt_1. The microstructure studies show that the absence of inclusions and the non-deflection of the foliations (S_1 and S_2) in most of the Grt_2 porphyroblasts indicate a late to post-deformation growth (Fig. 9d). The compositional profile of these garnets suggests progressive syn-metamorphic growth (temperatures obtained indicate 627 to 633 °C at the rim), and this temperature increase may have been induced by the granite intrusion in the deposit lithologies (Fig. 2a) at the end of the D_2 Archean deformation event.

Grt_3 is the youngest garnet generation and has a wide spatial distribution, and its size is significantly less than that of Grt_1 and Grt_2. The Grt_3 also lacks inclusions or considerable compositional zoning and is interpreted as post-deformation with respect to D_2 (Fig. 9e). The temperature calculated for the rims of Grt_3 is lower (518 to 537 °C) than that for all other garnet generations. They probably grew during the onset of cooling after D_2 (during D_3?), possibly due to retrograde re-equilibration, which could be relatively strong in these small grains.

Structural evolution of the Turmalina deposit

The geological evolution of the Turmalina deposit (Fig. 10) includes a three-stage deformation history (Table 2): D_1 and D_2, responsible for the progressive deformation during the Archean tectonic event, and D_3, which is a younger event but probably still Archean in age. The Brasiliano orogenic event (630–480 Ma; Pedrosa-Soares et al. 2011), which affected the rocks of the Minas and Rio das Velhas supergroups in the east of the QF, is not documented in the Precambrian rocks of the Turmalina deposit.

The D_1 event is interpreted as the result of progressive regional shearing with N-S shortening. The structures contain E-W trending, S-verging regional isoclinal folds (F_1), and a pervasive, continuous S_1 foliation that commonly obliterates the primary compositional banding. The V_{1-2} veins and their geometry match the orientation of the kilometer-scale faults and shear zones (D_1 from Baltazar and Zucchetti 2007), which leads to the interpretation that the formation of these veins started after 2749 ± 7 Ma (Hartmann et al. 2006; the U-Pb SHRIMP age of the youngest detrital zircon, which limits the deposition of the Nova Lima Group) and before ~2700 Ma (Noce et al. 2007; the age of the second granitic magmatic episode).

With the progressive continuation of the deformation, a second generation of structures (D_2 deformation event) is

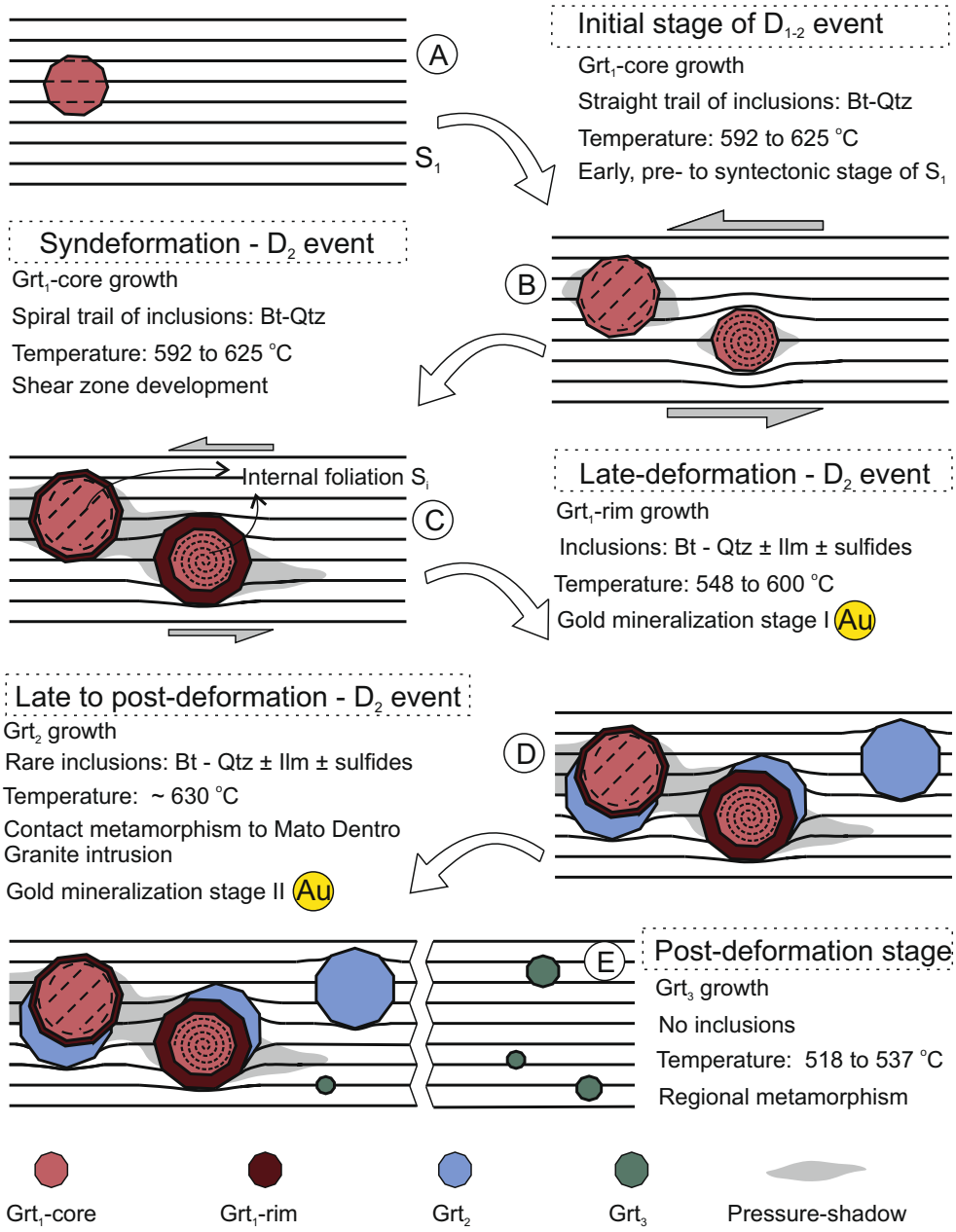

Fig. 9 Schematic diagram illustrating the timing relationships of the garnet porphyroblasts related to deformation events and gold mineralization stages

associated with left-lateral shear zones that nucleated parallel to the axial plane of the F_1 folds. The Ls_2 mineral and stretching lineation plunges to the ESE and formed in response to the continued development of the foliation (S_1) during ductile shearing. These conditions were also responsible for the development of the mica fish structures and S-C fabric, with their orientation indicating a sinistral sense of movement for the shear zones. The S_1 foliation strikes consistently NW-SE and dips (except in the inflection of orebody B) at a high angle to the NE, whereas the lineation Ls_2 plunges SE. This indicates oblique transportation of the hanging wall to WNW, probably under transpressive conditions and showing sinistral shear sense. The Ls_2 stretching lineation, the *X*-axis of boudins and the axis of pinch-and-swell structures of the veins define the direction of the principal stretching (Ls_2 is parallel to displacement vector) in the host rocks during D_2. Thus, in the shear planes, the high gold content of the orebodies follows the orientation of these veins, as shown in detail in Fig. 11. Transpression may also have been responsible for the formation of F_2 folds and S_2 crenulation cleavage particularly in the bifurcation area of the veins that apparently were a focus of heterogeneous shortening and development of meter-scale folds.

The D_1 and D_2 events have progressively developed during an orogenic event that is bracketed between 2749 ± 7 Ma (Hartmann et al. 2006) and 2664 ± 35 Ma (Tassinari et al. 2015), according to the age obtained for the crystallization of the intrusive granite from the Mato Dentro Intrusive

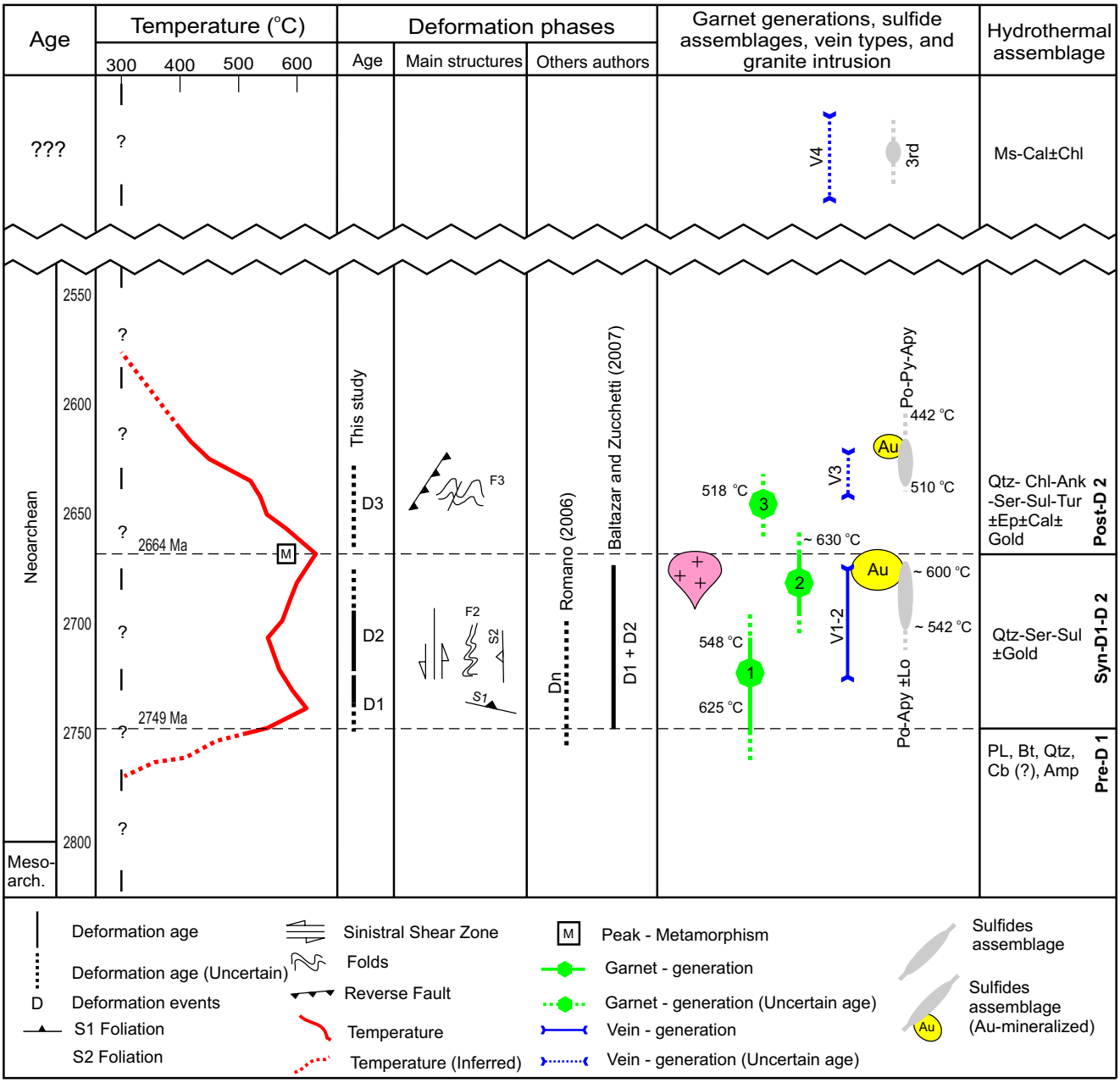

Fig. 10 Structural evolution of the Turmalina deposit, considering deformation and intrusive events, vein generations, hydrothermal phases, garnet growth, and gold mineralization stages. The temperatures were derived from garnet-biotite and arsenopyrite geothermometry. See also the comparison with structural evolution of other authors (indicated in the figure and shown in ESM Table 1). Ank ankerite, Cal calcite, Chl chlorite, Ep epidote, Ms muscovite, Qtz quartz, Ser sericite, Sul sulfide, Tur tourmaline

Suite. This interpretation appears consistent with the interpretations of Baltazar and Zucchetti (2007) for the Rio das Velhas Supergroup (in the eastern part of the QF).

The D_3 structures are interpreted as the result of the continuous activity of transpressional Archean deformation under ductile-brittle conditions associated with the regional NE-SW-trending sinistral shear zone. The structural elements are represented mainly by open, asymmetrical F_3 folds with sheared flanks (axial planes dip steeply NE and the axes plunge NW), associated with the conjugate, ESE-WNW-striking, reverse faults and NW-SE-striking reverse faults. The age of this deformation event is contentious, and the hypothesis of D_3 being of the Riacian-Orosirian event (Brito Neves 2011) cannot be excluded. Tassinari et al. (2015) proposed that structural evolution at Turmalina was developed during the Riacian-Orosirian (starting at the time when the shear zones cross-cut the host rocks, between 2.2 and 2.1 Ga, and terminated with the late hydrothermal influx post 1.75 Ga), although the influence of Paleoproterozoic deformation is not well

Table 2 Structural evolution of the Turmalina deposit

Age (Ma)	Tectonic event	Chronological deformation events	Kinematics	Structures
After 2749 (1) and before ~2700 (2)	Archean	D_1	Transport N to S	- Isoclinal F1 folds - Axial-planar S_1 foliation (E-W axial trace)
Before 2664 (3)	Archean	D_2	Transport NNE to SSW	- E-W striking, left lateral shear zones - V_{1-2} veins - Down-dip stretching and mineral lineation L_1 (30/90) - NNW-SSE to NNE-SSW striking S_2 crenulation cleavage - L_2 crenulation lineation plunging towards 280–317 - F_2 fold, axial-plane subparallel to S_2
After 2664 (3)	Archean (?)	D_3	Transcurrent NE-SW	- F_3 fold axes, plunged towards to NW - V_3 veins - NW-striking, NE-verging reverse faults - WNW-striking, SW and NE-verging reverse faults

The geochronological data are from (1) Hartmann et al. (2006), (2) Baltazar and Zucchetti (2007), and (3) Tassinari et al. (2015)

documented in the northwest of the Quadrilátero Ferrífero (Heineck 1997; Romano et al. 1995). In addition, the NW-vergent structures, described by Alkmim and Marshak (1998) for the Paleoproterozoic supracrustal sequences of the Minas Supergroup (in the eastern region of the QF), are not consistent with the D_3 kinematics determined here. Alternatively, the D_3 event could be related to a younger regional metamorphic phase of the Riacian-Orosirian event, suggested by age dates (2148 Ma, Sm-Nd whole rock age) of Tassinari et al. (2015).

Hydrothermal alteration and the timing of mineralization stages

At Turmalina, hydrothermal processes are considered to have developed mainly during the Archean tectonic event, which influenced the style of mineralization and permeability of, and fluid flow in, the rocks. There are six main hydrothermal alteration minerals that affect the rocks of the deposit. The alteration is accompanied with an addition of quartz, sulfide, carbonate, chlorite, tourmaline, and sericite that is distributed

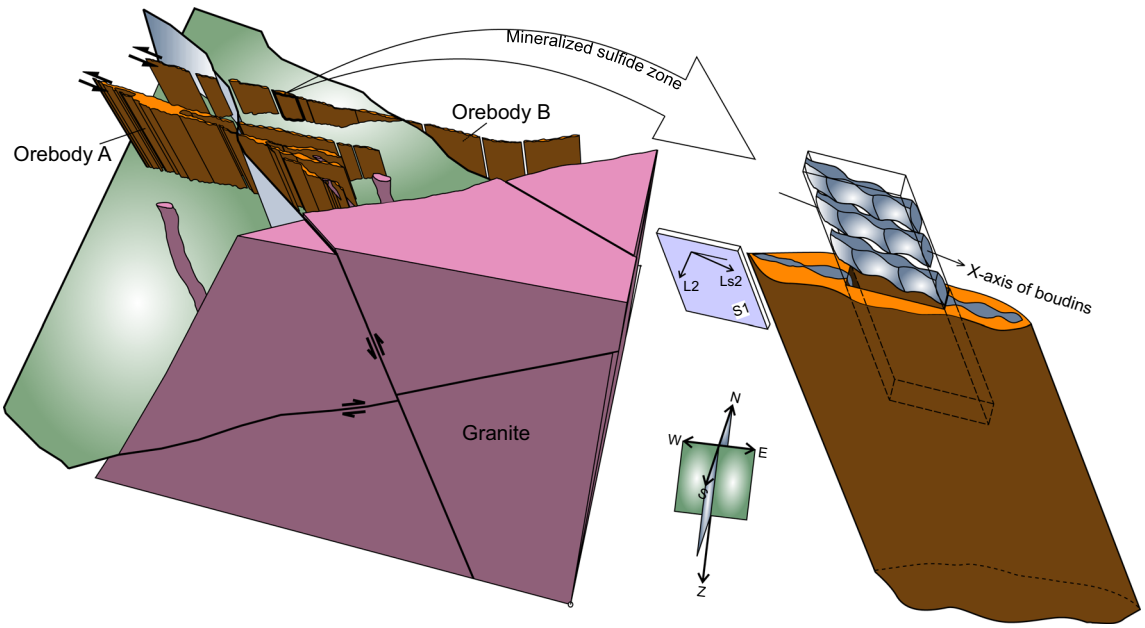

Fig. 11 Structural control of orebodies A and B in the Turmalina deposit showing the mineralized sulfide zone (orange), controlled by sinistral shear zones. The blow-up of the part of orebody B (right side) shows boudin-aged V_{1-2} veins with *X*-axes parallel to the stretching lineation Ls_2, which define the plunge of the mineralization. Representative reverse faults of the second-generation G_2 are shown as green (first population of faults) and blue (second population of faults) surfaces

in zones enveloping the orebodies (Table 1). The silicification is the dominant hydrothermal alteration process and is related to hydrothermal brecciation and vein network formation. The sulfide assemblages from the mineralization stages are cogenetic with the silicification, which defines the orebodies. Sulfidation is limited to a narrow zone (3 to 7 m wide) adjacent to the shear zone (mineralized sulfide zone; Fig. 7). Around the veins, which are parallel to the S_1 foliation, this halo is approximately symmetric, suggesting that fluid percolation was guided by the host rock foliation. Finally, tourmaline is encountered exclusively in narrow bands in mineralized zones or adjacent to them and chlorite has a wider distribution. The abundance of chlorite increases slightly in the proximal alteration zone.

The polyphase hydrothermal alteration history

Based on mineralogical features and diagnostic textures, at least three hydrothermal phases have been identified at Turmalina (see the last column of the Fig. 10), the first two associated with gold (mineralization stages I and II). Although the mafic-ultramafic unit is also altered by hydrothermal minerals (such as quartz, sericite, and chlorite), it does not host the orebodies and is, therefore, not discussed in this study.

An early phase of hydrothermal alteration, synchronous to mineralization stage I, is recorded by a quartz-sericite-sulfide assemblage in the volcano-sedimentary unit. This phase is characterized by sericite related to the destabilization of feldspar and the intense silicification of the host rocks, identified by a 3-7-m-wide network of quartz veins and hydraulic breccias. This alteration is overprinted by a second quartz-chlorite-ankerite-sericite-sulfide-tourmaline ± epidote ± calcite ± gold alteration phase (responsible for gold mineralization stage II). This second phase is represented mainly by an initial quartz, sulfide recrystallization, generation of the V_3 veins, and then massive chlorite bands in the proximal alteration zone. The hydrothermal fluids from the second alteration phase are interpreted as a product of the continuous development of the shear zones, via a new hydrothermal pulse (with increased fluid volume, perhaps related to the dehydration of host rocks caused by the ascent of a granite). The final phase of hydrothermal alteration recognized at Turmalina is associated with a muscovite-calcite-chlorite assemblage and the formation of the barren V_4 quartz veins. Based on overprinting relationships, the final phase postdates the two mineralization stages.

The gold-bearing sulfides and the timing of metamorphic minerals

The sulfidation process affecting the metamorphic assemblages indicates that (i) the pyrrhotite-arsenopyrite ± löllingite ± chalcopyrite assemblage from mineralization stage I (linked to the development of S_1 foliation) is in equilibrium with garnet Grt_1 (rarely Grt_2) and staurolite from the staurolite-garnet-ilmenite ± titanite paragenetic stage, (ii) the pyrrhotite-pyrite-arsenopyrite ± chalcopyrite assemblage from mineralization stage II is related to metamorphic assemblage of garnet-epidote ± chlorite ± rutile paragenetic stage, and (iii) the development of muscovite-calcite-chlorite hydrothermal alteration assemblage is associated with a late pyrite-pyrrhotite assemblage (synchronously with the development of V_4 veins?), but its chronological relationship could not be defined.

The hydrothermal assemblages in the Turmalina gold deposit overgrow and replace the metamorphic mineral assemblage, as also documented from other orogenic Archean gold deposits (e.g., Groves and Foster 1993; Junqueira et al. 2007). The presence of pyrrhotite-arsenopyrite ± löllingite inclusions in rims of garnets Grt_1 and Grt_2 suggests that gold in mineralization stage I, precipitated close to the metamorphic peak. In this case, stage I gold-bearing sulfide assemblage overprints the staurolite-garnet-ilmenite ± titanite metamorphic assemblages. The data obtained by arsenopyrite geothermometry indicate a temperature of 542 ± 30 to 598 ± 19 °C (Fig. 8) for the first assemblage of sulfides, slightly below the obtained metamorphic peak temperature of 627 to 633 °C (garnet-biotite geothermometry; ESM Fig. 4) on Grt_2 garnet rims.

The geothermometer obtained from gold mineralization stage II (arsenopyrite from the pyrrhotite-pyrite-arsenopyrite assemblage in V_3 veins) indicates a lower temperature of 442 ± 9 to 510 ± 30 °C (Fig. 8). The presence of epidote in equilibrium with arsenopyrite from gold mineralization stage II, although rare, suggests that the precipitation of these hydrothermal fluids continued towards temperatures still lower than 442 ± 9 °C (transition to epidote-amphibolite facies, around 450 °C; Bucher and Grapes 2011). The increasing amount of carbonate in V_3 veins related to the gold mineralization stage II may be explained by a progressive lowering of the temperature, which favors the stability of carbonate (Mikucki and Ridley 1993).

Considerations on the age of mineralization at Turmalina

Almost all orogenic gold deposits in the world are linked to three intervals in the geological time (Goldfarb et al. 2001; Tomkins 2013): (i) in the Neoarchean, between 2700 and 2400 Ma; (ii) in the Paleoproterozoic, between 2100 and 1800 Ma; or (iii) around 650 Ma, continuing through the Phanerozoic. In the QF, the most robust data on the age of gold mineralization were obtained in the deposits of Morro Velho and Cuiabá (2672 ± 14 Ma; Lobato et al. 2007) and Lamego (2730 ± 42 Ma; Martins et al. 2015) using U-Pb SHRIMP dating of hydrothermal monazite in equilibrium with sulfides and gold. Some Pb-Pb model ages were obtained for other deposits, including Bela Fama (2710 Ma; Thorpe et al. 1984) and São Bento (2650 Ma; DeWitt et al. 2000).

Other authors, however, attribute a Paleoproterozoic age for mineralization using mainly Pb-Pb ages or relative timing (e.g., Vial et al. 2007b) based on the tectonic models of Alkmim and Marshak (1998) and others.

For the Turmalina deposit, Tassinari et al. (2015) argue for a unique Paleoproterozoic tectonic evolution and mineralization age. Their interpretation is mainly based on Sm-Nd dating of garnets (between 2.2 and 2.1 Ga) and Rb-Sr dating of muscovite (1929 ± 17 Ma), in equilibrium with pyrite-arsenopyrite-gold and Pb-Pb isotopes in arsenopyrite (1946 ± 24 Ma).

However, a single Paleoproterozoic age of gold mineralization at Turmalina is incompatible, considering the geological, microtextural, and thermometric data presented here, as well as U-Pb SHRIMP age on zircon in an intrusive granite stock (2664 ± 35 Ma; Tassinari et al. 2015). The gold-bearing veins are synchronous with the main foliation (S_1) developed during D_1, which is responsible for the ore-controlling structures in Turmalina, and they clearly precede the granitic intrusion (as seen in Fig. 2b and ESM Fig. 2g). Among the two gold mineralization stages, the first (pyrrhotite-arsenopyrite ± löllingite ± chalcopyrite) assemblage shows a strong genetic relationship with the main S_1 foliation of pre-granite, Archean age. The second (pyrrhotite-pyrite-arsenopyrite ± chalcopyrite) assemblage is interpreted also of Archean age, related to a second hydrothermal fluid pulse that caused the recrystallization of pyrrhotite-arsenopyrite and new crystallization of sulfide grains in the V_3 quartz veins.

Comparison between Turmalina and other gold deposits in the QF: the source of gold and the sulfur isotope data

The $\delta^{34}S$ data for arsenopyrite, pyrite, and pyrrhotite show a range from + 2.94 to + 5.76‰ V-CDT (ESM Table 5; Fig. 12). These $\delta^{34}S$ values alone could be interpreted either as metamorphic fluid derived or, alternatively, as related to felsic-intermediate, mantle-derived magmas (cf. Sakai et al. 1984). For other Au deposits in the QF (Fig. 12), a metamorphic origin of the mineralizing fluid is widely accepted (Lobato et al. 2001; Bühn et al. 2012; Ribeiro et al. 2015). Bühn et al. (2012), based on S isotopes in the São Bento and Cuiabá gold deposits, suggested that the sulfur was remobilized from the greenstone belt sequence. Ribeiro et al. (2015) arrive at a similar conclusion for the Carvoaria Velha deposit, which suggests that the mineralizing fluids derived from metamorphic dehydration and subsequent interaction with the volcano-sedimentary sequence during its ascent.

In such a context, the sedimentary and volcano-sedimentary rocks, including carbonaceous layers as described by Romano (2006) that occur at the base of the Nova Lima Group in the

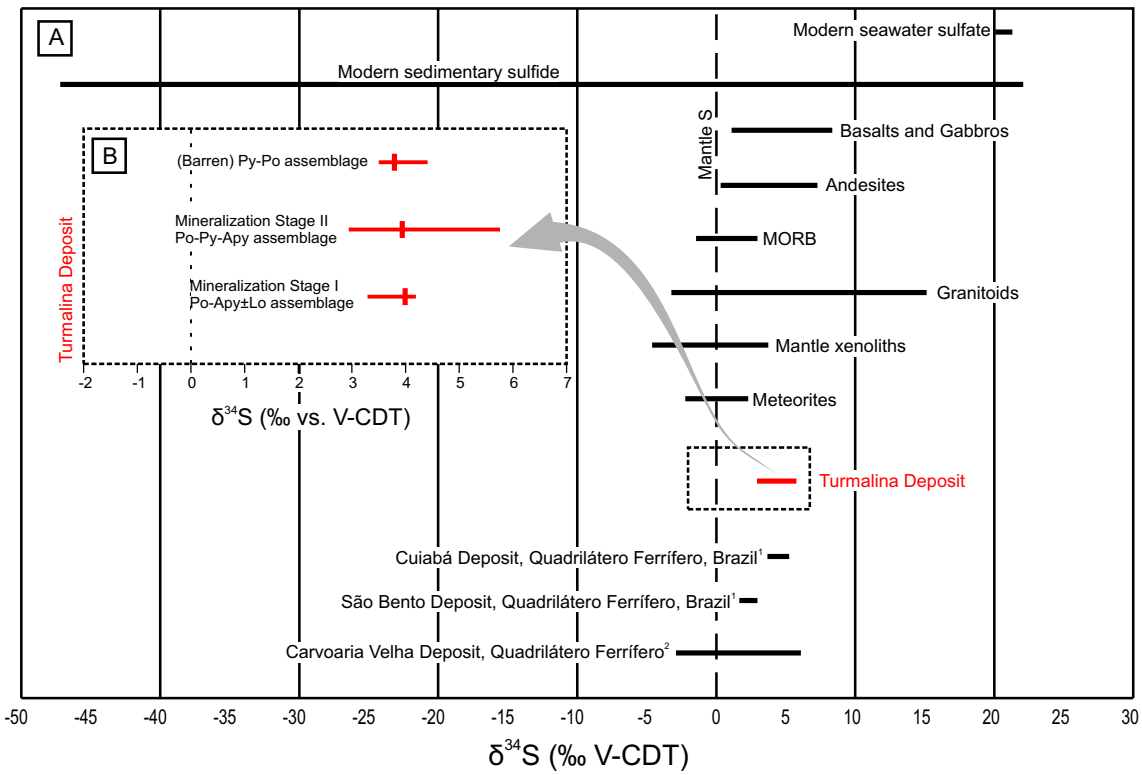

Fig. 12 **a** Sulfur isotope composition of Turmalina sulfides compared with other Archean gold deposits of the QF, and sulfur from the mantle and crustal rocks. Adapted from Seal (2006), with data of Sasaki and Ishihara (1979), Chambers (1982), Rye et al. (1984), Farquhar et al. (2002), Bühn et al. (2012)[1], and Ribeiro et al. (2015)[2]. **b** Detail of sulfur isotopic compositions of the three sulfide assemblages from Turmalina. Apy arsenopyrite, Lo löllingite, Py pyrite, Po pyrrhotite

northwestern part of the QF region, may be considered as one of the sources for the mineralizing hydrothermal fluid. However, the hydrothermal mineralization may also be related (at least in part) by the intrusion of the granite, which could have imposed an additional thermal effect promoting further dehydration of the country rocks. Alternatively, the high temperatures recorded for the mineralization stages at the Turmalina deposit (relative to those obtained from the Carvoaria Velha, São Bento, and Cuiabá deposits, for example) and the nearby granitic intrusion may suggest a possible igneous origin for, at least partially, the mineralizing fluids of this deposit. In this context, the granite potentially also contributed to the metal budget but additional stable and radiogenic isotopic studies are necessary to confirm this hypothesis.

Conclusions

The Turmalina gold deposit is located in Archean rocks belonging to the base of the Rio das Velhas Supergroup (or correlated sequence) metamorphosed under amphibolite facies conditions. From bottom to top, the lithostratigraphy is defined by an ortho-amphibolite (mafic-ultramafic unit) followed by a volcano-sedimentary sequence with metapelites and intercalated meta-tuffs. A granite from the Mato Dentro Intrusive Suite intruded the host rocks in the deposit (ESM Fig. 1).

The structural development of the deposit is characterized by a progressive Archean event (D_1 and D_2) related to large-scale structures and a subsequent D_3 event (Fig. 3). The D_1 event occurred at an initial stage of N-S shortening and kinematic indicators rotated towards NNE-SSW during D_2, which developed the ductile shear zones that control the orebodies. This event is temporally confined between the development of regional faults (2749 Ma), defined by Romano (2006) and discussed by Baltazar and Zucchetti (2007), and the age of a granitic stock (2664 ± 35 Ma; Tassinari et al. 2015) that intrudes the deposit (Fig. 10). The D_3 event is interpreted as a transpressional, sinistral, event under ductile-brittle conditions.

Three generations of veins were identified (Fig. 5): $V_{1–2}$, V_3, and V_4, the first two contain gold. The gold is mainly located in thin bands within sulfides or in massive sulfide aggregates at the edges of $V_{1–2}$ veins. The V_3 veins are related to the development of reverse faults and, microscopically, quartz and carbonate veinlets that truncate the main foliation. Finally, V_4 veins occur as thin milky quartz veins with no preferred orientation and are not mineralized.

Detailed petrographic, mineral chemistry, and structural analyses identified three sulfide-bearing assemblages, the first two being gold bearing (gold mineralization stages I and II). The first sulfide assemblage (pyrrhotite-arsenopyrite ± löllingite ± chalcopyrite) from gold mineralization stage I precipitated near the metamorphic peak temperatures of initially about 630 °C, then decreasing to 540 °C, and is closely related to the development of D_2 structures (Figs. 8 and 10). The post-metamorphic, second assemblage (pyrrhotite-pyrite-arsenopyrite ± chalcopyrite) from gold mineralization stage II overprints stage I. The mineralization stage II reached temperatures of 510 to 440 °C and is interpreted as being also of Archean age, although a younger, hydrothermal event during the Paleoproterozoic cannot be discarded. In combination, these observations constitute the first evidence for multiple stages of gold deposition in the NW part of the QF.

Garnet is an important mineral in Turmalina, which recorded the structural and metamorphic history in the different evolutionary stages of the deposit (Fig. 9, ESM Fig. 4). The Grt_1 is pre- to syn-deformation relative to the Archean tectonic event. The precipitation of the first generation of sulfide occurred before the end of its growth. Garnet-biotite geothermometry suggests that garnet crystallized under retrograde metamorphic conditions (up to 625 °C in the core and to 548 °C at the rims), with the end of its blastesis associated with the end of the tectonic event. The Grt_2 is associated with the emplacement and uplift of a granitic stock into the host rocks. This garnet is late to post-deformation with respect to the D_2 event and took place during reheating in a second phase of metamorphism. The sulfides of the gold mineralization stage I indicate that the mineralization process continued with post-Grt_2 cooling to near 510 °C.

We suggest that the hydrothermal fluids responsible for mineralization in the Turmalina deposit are derived from the dehydration of rocks from the base of the Rio das Velhas, favored by the increased temperatures during the emplacement of the granite stock into these host rocks.

Acknowledgements The authors wish to acknowledge the Jaguar Mining Co. for their technical, logistic, and financial support during our research. Special thanks to Carlos Ribeiro Luiz and all technicians, helpers, and geologists in the Turmalina Mine: Williams Santos, Romulo Cruz, Carlos Michel, Alvania Augusta, Armando Filho, Lucas, and Aloma Tente. Numerous geologists and many people must be thanked for their support and discussions: Ana-Sophie Hensler, Fabrício Caxito, Atlas Corrêa-Neto, Haakon Fossen, Lydia Lobato, Jaqueline Menez, Ruy Vasconcelos, William Campos, and Maria Emília Della Giustina. We thank the Mineralium Deposita reviewers (Dr. Ridley and Dr. Micklethwaite) and the AE (Dr. Steffen Hagemann) for providing constructive and helpful comments. We also acknowledge the support of Brasilia University, UnB, which improved the conditions to do electron microprobe analyses and LA-ICP-MS.

Note: It is with a certain sense of sadness that we report the passing of Dr. Bernhard Bühn. Bernhard is a true scholar and a gentleman. He was a pioneer in the UnB's geochronology laboratory, especially for the ICP-MS method, and left a great legacy.

Funding information This research is financed by Brazil's Personal Improvement Coordination of Higher Education, CAPES.

References

Alkmim FF, Marshak S (1998) Transamazonian orogeny in the southern São Francisco Craton region, Minas Gerais, Brazil: evidence for Paleoproterozoic collision and collapse in the Quadrilátero Ferrífero. Precambrian Res 90:29–58

Almeida FFM (1977) O Cráton do São Francisco. Rev Bras Geosci 7: 349–364

Baltazar OF, Zucchetti M (2007) Lithofacies associations and structural evolution of the Archean Rio das Velhas greenstone belt, Quadrilátero Ferrífero, Brazil: a review of the setting of gold deposits. Ore Geol Rev 32:471–499

Berman RG (1991) Thermobarometry using multi-equilibrium calculations: a new technique, with petrological applications. Can Mineral 29:833–855

Brito Neves BB (2011) The Paleoproterozoic in the South-American continent: diversity in the geologic time. J S Am Earth Sci 32: 270–286

Bucher K, Grapes R (2011) Metamorphic grade. In: Petrogenesis of metamorphic rocks. Springer, Berlin, pp 119–187

Bühn B, Santos RV, Dardenne MA, de Oliveira CG (2012) Mass-dependent and mass-independent sulfur isotope fractionation (δ34S and δ33S) from Brazilian Archean and Proterozoic sulfide deposits by laser ablation multi-collector ICP-MS. Chem Geol 312–313:163–176

Caddick MJ, Konopásek J, Thompson AB (2010) Preservation of garnet growth zoning and the duration of prograde metamorphism. J Petrol 51:2327–2347

Chambers LA (1982) Sulfur isotope study of a modern intertidal environment, and the interpretation of ancient sulfides. Geochim Cosmochim Acta 46:721–728

Cooke RA, O Brien PJ, Carswell DA (2000) Garnet zoning and the identification of equilibrium mineral compositions in high-pressure-temperature granulites from the Moldanubian Zone, Austria. J Metamorph Geol 18:551–570

DeWitt E, Thorman C, Ladeira E et al (2000) Origin and age of gold deposits at São Bento and Morro Velho, Brazil. 31th Internat Geol Congress, Rio de Janeiro, Brazil, CD-ROM

Dorr JVN (1957) In: DNPM M (ed) Revisão da Estratigrafia Précambriana do Quadrilátero Ferrífero: Brasil. Departamento Nacional de Produção Mineral, Minas Gerais 81 p

Dorr JVN (1969) Physiographic, stratigraphic and structural development of the Quadrilátero Ferrífero, Minas Gerais, Brazil. Regional Geology of the Quadrilátero Ferrífero, Minas Gerais, Brazil. US Geol Surv Professional Paper 614-A. 110 p

Farquhar J, Wing BA, McKeegan KD, Harris JW, Cartigny P, Thiemens MH (2002) Mass-independent sulfur of inclusions in diamond and sulfur recycling on early Earth. Science 298:2369–2372

Frizzo C, Takai V, Scarpelli W (1991) Auriferous mineralization at Pitangui, Minas Gerais. In: Ladeira EA (ed) Brazil Gold '91. Balkema, Rotterdam, pp 579–583

Goldfarb RJ, Groves DI, Gardoll S (2001) Orogenic gold and geologic time: a global synthesis. Ore Geol Rev 18:1–75

Groves DI, Foster RP (1993) Archean lode gold deposits. In: Foster RP (ed) Gold metallogeny and exploration. Chapman and Hall, New York, pp 63–103

Hartmann LA, Endo I, Suita MTF, Santos JOS, Frantz JC, Carneiro MA, McNaughton NJ, Barley ME (2006) Provenance and age delimitation of Quadrilátero Ferrífero sandstones based on zircon U-Pb isotopes. J Am Earth Sci 20:273–285

Heineck CA (1997) Geologia e mineralizações do Greenstone Belt Rio das Velhas na região de Mateus Leme, Minas Gerais. Dissertation, UFMG, Belo Horizonte, Brazil

Inda HV, Schorscher HD, Dardenne MA et al (1984) O cráton do São Francisco e a Faixa de Dobramento Araçuaí. In: Schobbenhaus C, Campos DA, Derze GR, Asmus HE (eds) Geologia do Brasil—Texto explicativo do mapa geológico do Brasil e área oceânica adjacente. MME/DNPM, Brasília, pp 193–248

Jaguar Mining Inc (2017) www.jaguarmining.com/operations/turmalina-gold-mine/. Accessed 17 Jun 2017

Junqueira P, Lobato L, Ladeira E, Simões E (2007) Structural control and hydrothermal alteration at the BIF-hosted Raposos lode-gold deposit, Quadrilátero Ferrífero Brazil. Ore Geol Rev 32:629–650

Kretschmar U, Scott SD (1976) Phase relations involving arsenopyrite in the system Fe–As–S and their application. Can Mineral 14:364–386

Ladeira E (1980) Geology, petrography, and geochemistry of Nova Lima Group, Quadrilátero Ferrífero, Minas Gerais, Brasil. XVII Geowiss Lateinamer Kolloq, Heidelberg, pp 47–48

Lobato LM, Ribeiro-Rodrigues LC, Vieira FWR (2001) Brazil's premier gold province. Part II: geology and genesis of gold deposits in the Archean Rio das Velhas greenstone belt, Quadrilátero Ferrífero. Mineral Deposita 36:249–277

Lobato LM, Santos J, McNaughton N et al (2007) U–Pb SHRIMP monazite ages of the giant Morro Velho and Cuiabá gold deposits, Rio das Velhas greenstone belt, Quadrilátero Ferrífero, Minas Gerais, Brazil. Ore Geol Rev 32:674–680

Machado N, Carneiro MA (1992) U–Pb evidence of Late Archean tectonothermal activity in the southern São Francisco shield, Brazil. Can J Earth Sci 29:2341–2346

Machado N, Noce CM, Oliveira OAB, Ladeira EA (1989) Evolução Geológica do Quadrilátero Ferrífero no Arqueano e Proterozóico Inferior com Base em Geogronologia U–Pb. In: SBd G (ed) Anais do V Simpósio de Geologia de Minas Gerais. Núcleo Minas Gerais, Belo Horizonte, pp 1–4

Martins BS, Lobato LM, Rosière CA et al (2015) The Archean BIF-hosted Lamego gold deposit, Rio das Velhas greenstone belt, Quadrilátero Ferrífero: evidence for Cambrian structural modification of an Archean orogenic gold deposit. Ore Geol Rev 72:963–988

Mikucki EJ, Ridley JR (1993) The hydrothermal fluid of Archaean lode-gold deposits at different metamorphic grades: compositional constraints from ore and wallrock alteration assemblages. Mineral Deposita 28:469–481

Noce CM, Tassinari CG, Lobato LM (2007) Geochronological framework of the Quadrilátero Ferrífero, with emphasis on the age of gold mineralization hosted in Archean greenstone belts. Ore Geol Rev 32:500–510

Noce CM, Machado N, Teixeira W (1998) U–Pb geochronology of gneisses and granitoids in the Quadrilátero Ferrífero (southern São Francisco Craton): age constraints for Archean and Paleoproterozoic magmatism and metamorphism. Rev Bras Geosci 28:95–102

Oliveira MS (2012) Rochas hospedeiras e alteração hidrotermal associadas às mineralizações auríferas dos corpos Turmalina e Satinoco, mina de ouro de Turmalina, Pitangui (MG). Trabalho de conclusão de curso, Universidade Estadual de Campinas

Pedrosa-Soares A, De Campos CP, Noce C et al (2011) Late Neoproterozoic-Cambrian granitic magmatism in the Araçuaí orogen (Brazil), the Eastern Brazilian Pegmatite Province and related mineral resources. Geol Soc Lond Spec Publ 350:25–51

Petrakakis K (1986) Metamorphism of high-grade gneisses from the Moldanubian Zone, Austria, with particular reference to the garnets. J Metamorph Geol 4:323–344

Renger FE, Noce CM, Romano AW, Machado N (1994) Evolução sedimentar do Supergrupo Minas: 500 Ma de registro geológico no Quadrilátero Ferrífero, Minas Gerais, Brasil. Geonomos – Rev Bras Geosci 2:1–11

Ribeiro Y, Figueiredo e Silva RC, Lobato LM, Lima LC, Rios FJ, Hagemann SG, Cliff J (2015) Fluid inclusion and sulfur and oxygen isotope studies on quartz–carbonate–sulfide veins of the Carvoaria Velha deposit, Córrego do Sítio gold lineament, Quadrilátero Ferrífero, Minas Gerais, Brazil. Ore Geol Rev 67:11–33

Romano AW (1989) Evolution Tectonique de la région Nord-Ouest du Quadrilatère Ferrifère-Minas Gerais-Brésil. PhD Thesis, Université de Nancy I, Vandoeuvre-lès-Nancy, France

Romano AW (2006) Programa Geologia do Brasil. Folha Pará de Minas, SE-23-Z-C-I. Escala 1:100.000 relatório final. UFMG-CPRM, Belo Horizonte. 74 pp

Romano AW, Bilal E, Correa Neves JM et al (1995) O Complexo Granítico de Florestal-parte meridional do Cráton de São Francisco—primeiros dados petrográficos e geoquímicos. In: Simp Geol MG, 8. Diamantina. SBG/MG 13:86–88

Rye RO, Luhr JF, Wasserman MD (1984) Sulfur and oxygen isotope systematics of the 1982 eruptions of El Chichón volcano, Chiapas, Mexico. J Volcanol Geotherm Res 23:109–123

Sakai H, Des Marais DJ, Ueda A, Moore JG (1984) Concentrations and isotope ratios of carbon, nitrogen and sulfur in ocean-floor basalts. Geochim Cosmochim Acta 48:2433–2441

Sasaki A, Ishihara S (1979) Sulfur isotopic composition of the magnetite-series and ilmenite-series granitoids in Japan. Contrib Mineral Petrol 68:107–115

Schorscher HD (1978) Komatiítos na estrutura "Greenstone Belt" Série Rio das Velhas, Quadrilátero Ferrífero, Minas Gerais, Brasil. XXX Congresso Brasileiro de Geologia. SBG, Recife, pp 292–293

Seal RR (2006) Sulfur isotope geochemistry of sulfide minerals. Rev Mineral Geochem 61:633–677

Sharp ZD, Essene EJ, Kelly WC (1985) A re-examination of the arsenopyrite geothermometer: pressure considerations and applications to natural assemblages. J Miner Assoc Canada 23:517–534

Soares MB, Corrêa-Neto AV, Zeh A, Cabral AR et al (2017) Geology of the Pitangui greenstone belt, Minas Gerais, Brazil: stratigraphy, geochronology and BIF geochemistry. Precambriam Res 291:17–41

Tassinari CCG, Mateus AM, Velásquez ME, Munhá JMU, Lobato LM, Bello RM, Chiquini AP, Campos WF (2015) Geochronology and thermochronology of gold mineralization in the Turmalina deposit, NE of the Quadrilátero Ferrífero Region, Brazil. Ore Geol Rev 67: 368–381

Thorman CH, DeWitt E, Maron MA, Ladeira EA (2001) Major Brazilian gold deposits—1982 to 1999. Mineral Deposita 36:218–227

Thorpe RI, Cumming GL, Krstic D (1984) Lead isotope evidence regarding age of gold deposits in the Nova Lima district, Minas Gerais, Brazil. Rev Bras Geosci 14:147–152

Tomkins AG (2013) On the source of orogenic gold. Geology 41:1255–1256

Tuccillo ME, Essene EJ, Van Der Pluijm BA (1990) Growth and retrograde zoning in garnets from high-grade, metapelites: implications for pressure-temperature paths. Geology 18:839–842

Velasquez David ME (2011) Evolução Termocronológica e Metalogenética da Mineralização Aurífera do Depósito Turmalina, Quadrilátero Ferrífero, Minas Gerais. PhD Thesis, Institute of Geosciences, University of São Paulo

Vial D, Abreu G, Schubert G, Ribeiro-Rodrigues L (2007a) Smaller gold deposits in the Archean Rio das Velhas greenstone belt, Quadrilátero Ferrífero, Brazil. Ore Geol Rev 32:651–673

Vial D, Duarte B, Fuzikawa K, Vieira M (2007b) An epigenetic origin for the Passagem de Mariana gold deposit, Quadrilátero Ferrífero, Minas Gerais, Brazil. Ore Geol Rev 32:596–613

Yardley BWD (1977) An empirical study of diffusion in garnet. Am Mineral 62:793–800